Impact of Combined Assimilation of Radar and Rainfall Data on Short-Term Heavy Rainfall Prediction: A Case Study

JUANZHEN SUN, YING ZHANG, AND JUNMEI BAN

National Center for Atmospheric Research, Boulder, Colorado

JING-SHAN HONG

Central Weather Bureau, Taipei, Taiwan

CHUNG-YI LIN

Taiwan Typhoon and Flood Research Institute, Taipei, Taiwan

(Manuscript received 11 October 2019, in final form 12 February 2020)

ABSTRACT

Radar and surface rainfall observations are two sources of operational data crucial for heavy rainfall prediction. Their individual values on improving convective forecasting through data assimilation have been examined in the past using convection-permitting numerical models. However, the benefit of their simultaneous assimilations has not yet been evaluated. The objective of this study is to demonstrate that, using a 4D-Var data assimilation system with a microphysical scheme, these two data sources can be assimilated simultaneously and the combined assimilation of radar data and estimated rainfall data from radar reflectivity and surface network can lead to improved short-term heavy rainfall prediction. In our study, a combined data assimilation experiment is compared with a rainfall-only and a radar-only (with or without reflectivity) experiments for a heavy rainfall event occurring in Taiwan during the passage of a mei-yu system. These experiments are conducted by applying the Weather Research and Forecasting (WRF) 4D-Var data assimilation system with a 20-min time window aiming to improve 6-h convective heavy rainfall prediction. Our results indicate that the rainfall data assimilation contributes significantly to the analyses of humidity and temperature whereas the radar data assimilation plays a crucial role in wind analysis, and further, combining the two data sources results in reasonable analyses of all three fields by eliminating large, unphysical analysis increments from the experiments of assimilating individual data only. The results also show that the combined assimilation improves forecasts of heavy rainfall location and intensity of 6-h accumulated rainfall for the case studied.

1. Introduction

Heavy rainfall is one of the most common high-impact weather phenomena across the globe and the most frequent cause of flooding, a hazard that results in significant loss of life and property damages each year. The prediction of heavy rainfall particularly in warm season, however, has been a long-standing scientific challenge in weather forecasting with slow progress. Since the warm season heavy rainfall is closely associated with mesoscale convective systems (Heideman and Fritsch 1984; Schumacher and Johnson 2005), the key to improving its prediction lies in developing convection-permitting numerical models that allow the representation of moist convection in these systems. Further, it is necessary for these models to be initialized by high-resolution (both in space and time) observations via rapid update data assimilation (DA) to keep up with the rapid evolvement of convection.

A major effort taken to improve short-term quantitative precipitation forecasts (QPFs) by both research and operational communities has been the assimilation of observations from Doppler radars (radial velocity and reflectivity) into convection-permitting models. While notable progress has been made (see Sun et al. 2014 for a review), challenges in heavy rainfall prediction are still plenty. Among many issues requiring future research and development is the assimilation of other high-resolution observations in addition to Doppler radars. For example, in recent years, efforts have been made to

Corresponding author: Juanzhen Sun, sunj@ucar.edu

DOI: 10.1175/MWR-D-19-0337.1

assimilate lightning observations (Fierro et al. 2012, 2014; Dixon et al. 2016) and geostationary satellite observations (Honda et al. 2018a,b; Zhang et al. 2018). Jones et al. (2015, 2016) investigated the impact of combined assimilation of radar and satellite observations of liquid/ice water path on severe storm prediction and found benefits comparing to the assimilation of any single type of the two data sources.

In this paper, our purpose is to demonstrate the benefit of assimilating rainfall analysis from quantitative precipitation estimation (QPE) simultaneously with radar radial velocity and reflectivity observations. QPE is a gridded hourly rainfall product derived from radar reflectivity observations (and polarimetric measurements in case of polarimetric radar) and surface rain gauge observations. The rainfall measurement from a surface rain gauge is commonly accepted as the ground truth of precipitation at a specific weather station; however, rain gauge networks cannot well represent the spatial distribution of rainfall over a region due to its limited station density. On the other hand, rainfall estimated from radar reflectivity has a high spatial resolution, but its accuracy is not as reliable as the rain gauge measurement because of its dependence on empirical relationship for the estimate. Hence, as NWP models are being run at increasingly higher resolutions, QPE products that combine a radar derived rainfall field and rain gauge measurements, taking advantages of the high resolution of the former and the higher accuracy of the latter, have become popular and are often used as the true rainfall field for verifying forecasts.

Strictly speaking, radar reflectivity and accumulated rainfall from QPE are not independent of each other because radar reflectivity is related to hydrometeors and rainfall is merely a temporal accumulation of the hydrometeors falling to the ground. Nevertheless, the two have distinct differences in that the former is a 3D snapshot related to hydrometeors via an assumed drop size distribution while the latter is a 2D hourly accumulated quantity obtained by an empirical Z–R relation. In addition, QPE is commonly adjusted by the independent measurements of surface rainfall from rain gauge networks. These differences could render different characteristics of the two quantities resulting in different outcomes of data assimilation. It is therefore worth examining the individual effects of the two data fields as well as their combined impact on data assimilation.

Although the effect of simultaneous assimilation of radar and rainfall data has not been evaluated, plenty of previous studies were conducted to assess the impact of radar observations or of rainfall observations (or QPE)[1] using three-dimensional and four-dimensional variational (3D-Var and 4D-Var) data assimilation techniques as well as ensemble Kalman filters (EnKF). It has been shown that the assimilation of the instantaneous three-dimensional reflectivity with a 3D-Var system is effective only if the dynamical field, such as latent heat or relative humidity, is forced to adjust via some simple assumptions on convective-scale dynamics, for instance, latent heat release or in-cloud saturation (e.g., Albers et al. 1996; Xue et al. 2003; Hu et al. 2006; Stephan et al. 2008; Weygandt et al. 2008; Wang et al. 2013a). Similarly, the rainfall observations have to be converted to latent heat release in a vertical column and then the latent heat can be assimilated into a model with a prespecified latent heat profile. Jones and Macpherson (1997) used this approach to assimilate QPE with a nudging technique.

Because the rainfall observations are accumulated in time, the four-dimensional data assimilation technique is in principle advantageous in assimilating these data due to the temporal window required to generate an analysis. Several previous studies demonstrated the effectiveness of the 4D-Var technique in rainfall data assimilation (Zou and Kuo 1996; Guo et al. 2000; Tsuyuki et al. 2002; Koizumi et al. 2005; Xu et al. 2006; Lopez and Bauer 2007; Lopez 2013). Recently the EnKF has also been applied to rainfall data assimilation (Miyoshi and Aranami 2006; Zupanski et al. 2011; Lien et al. 2013). To our knowledge, the only combined assimilation of both radar and rainfall data was done by the Met Office's 4D-Var. However, in their system, although the radar radial velocity is assimilated via the 4D-Var, the QPE data assimilation is done separately through the latent heat nudging method (Jones and Macpherson 1997) with prespecified vertical profiles (Ballard et al. 2015), partly due to the lack of the adjoint of microphysics in their 4D-Var.

In the current study, we use the Weather Research and Forecasting Data Assimilation (WRFDA) 4D-Var system (Huang et al. 2009; Wang et al. 2013b) to examine the impact of the combined assimilation of radar observations (radial velocity and reflectivity) and QPE. In the WRFDA 4D-Var system, the simultaneous assimilation of radar and rainfall data are made possible because of the microphysics scheme in its adjoint model. A number of previous studies have demonstrated the ability of the 4D-Var technique and its superior performance to its 3D-Var in improving convection-permitting model analyses and forecasts, for example, by Wang et al. (2013b),

[1] Although it is common to refer QPE as "rainfall analysis," in this paper we use "rainfall observation" to emphasize that it is the "observational" input data to be assimilated by the model.

Sun and Wang (2013), and Li et al. (2014) using WRFDA 4D-Var, by Kawabata et al. (2011) using the JMA (Japan Meteorological Agency) 4DVar system, and by Ballard et al. (2015) and Li et al. (2018) using Met Office's Unified Model 4D-Var. Our objective in the current study is to examine the relative contributions of the two most operationally available observation types for heavy rainfall forecasting, radar data and rainfall data, and to demonstrate that their combined assimilation produces improved convective-scale dynamical balance and hence improved short-term heavy rainfall prediction. A convective system imbedded in a mei-yu front occurred in Taiwan on 2 June 2017 is used for the DA and forecast experiments in our study. To achieve our objective, we will compare three experiments assimilating rainfall data only, radar data only (radial velocity and reflectivity), and all data (both radar and rainfall). To examine the impact of reflectivity when rainfall data are assimilated, an experiment assimilating radial velocity and rainfall is also conducted to be compared with the all data experiment.

The paper is organized as follows. In section 2 the WRFDA 4D-Var DA system is described. In section 3 the convective system of 2 June 2017 and the radar and rainfall observations are presented. Section 4 covers the configuration of the DA and modeling system and the experimental design. In section 5 we first present the results of four single observation experiments that perturb rainfall only, radial velocity and reflectivity, radial velocity and rainfall, and all three variables, respectively, and then the results of their real data experiments for the heavy rainfall case. A summary and conclusions are given in the last section.

2. Description of WRFDA 4D-Var

WRFDA is the variational DA system developed for WRF-ARW (Advanced Research Weather Research and Forecasting Model) (Skamarock et al. 2008), including both 3D-Var and 4D-Var. Huang et al. (2009) described the basic 4D-Var framework with the adjoint model (ADM) of WRF dynamical core. Zhang et al. (2013) described a major framework upgrade along with some other software enhancements. Wang et al. (2013b) developed the adjoint of a warm rain microphysical scheme and demonstrated its capability for radar DA. The assimilation of rainfall data was developed in recent years and described in Ban et al. (2017). Both the tangent linear model (TLM) and ADM of the 4D-Var system were upgraded over the years to match each of the updated WRF versions.

A 4D-Var DA system seeks an optimal analysis by iteratively reducing a cost function composed of a background term, an observations term, and a constraint term (i.e., $J = J_b + J_o + J_c$). The constraint term in WRFDA 4D-Var is a digital filter to prevent the analysis from contamination of high-frequency noise. With the objective to obtain an analysis x_0^a of the atmospheric state at a model initial time x_0, the background and the observation terms are defined as follows by assuming K observations with each represented by k:

$$J(x_0) = \frac{1}{2}(x_0 - x_0^b)^{\mathrm{T}}\mathbf{B}^{-1}(x_0 - x_0^b) + \frac{1}{2}\sum_{k=0}^{K}\{y_k^o - H_k[M_k(x_0)]\}^{\mathrm{T}}\mathbf{R}^{-1}\{y_k^o - H_k[M_k(x_0)]\}. \quad (1)$$

The variables of x_0^b and y_k^o represent the background state at the model initial time that is typically provided by a previous model forecast and the observed state, respectively; M_k is the nonlinear prediction model to propagate the initial atmospheric state to that at the kth observation time; H_k is the nonlinear observation operator at time k; and $\mathbf{B}$ and $\mathbf{R}$ are the background and observation error covariance matrices, respectively.

Similar to most of the operational variational DA systems, WRFDA 4D-Var is formulated by an incremental approach (Courtier et al. 1994) that converts the cost function (1) to one that uses increment (departure from nonlinear basic state) as the analysis control variable via the following variable transformation:

$$d_k = y_k^o - H_k[M_k(x_0)]. \quad (2)$$

Further, the nonlinear operators of H_k and M_k in Eq. (1) can be linearized as follows:

$$H_k[M_k(x_0^n)] \approx H_k[M_k(x_0^{n-1})] + \mathbf{H}_k\mathbf{M}_k[x_0^{n-1}]\delta x_0^n, \quad (3)$$

where the superscripts n and $n-1$ represent the current and previous outer loop iterations, respectively, and $\delta x_0^n = x_0^n - x_0^{n-1}$. Unlike the inner loop iterations that minimize the cost function, the outer loop iterations are performed to successively update the nonlinear basic state; $\mathbf{H}_k$ and $\mathbf{M}_k$ are the tangent linear operator of H_k and M_k. Applying Eqs. (2) and (3), the cost function (1) is changed to

$$J^n(\delta x_0^n) = \frac{1}{2}[\delta x_0^n - (x_0^b - x_0^{n-1})]^{\mathrm{T}}\mathbf{B}^{-1}[\delta x_0^n - (x_0^b - x_0^{n-1})] + \frac{1}{2}\sum_{k=0}^{K}[\mathbf{H}_k\mathbf{M}_k(x_0^{n-1})\delta x_0^n - d_0^{n-1}] \times \mathbf{R}^{-1}[\mathbf{H}_k\mathbf{M}_k(x_0^{n-1})\delta x_0^n - d_0^{n-1}]. \quad (4)$$

When the increment δx_0^n at the nth outer loop iteration is obtained, the estimate of the atmospheric state is

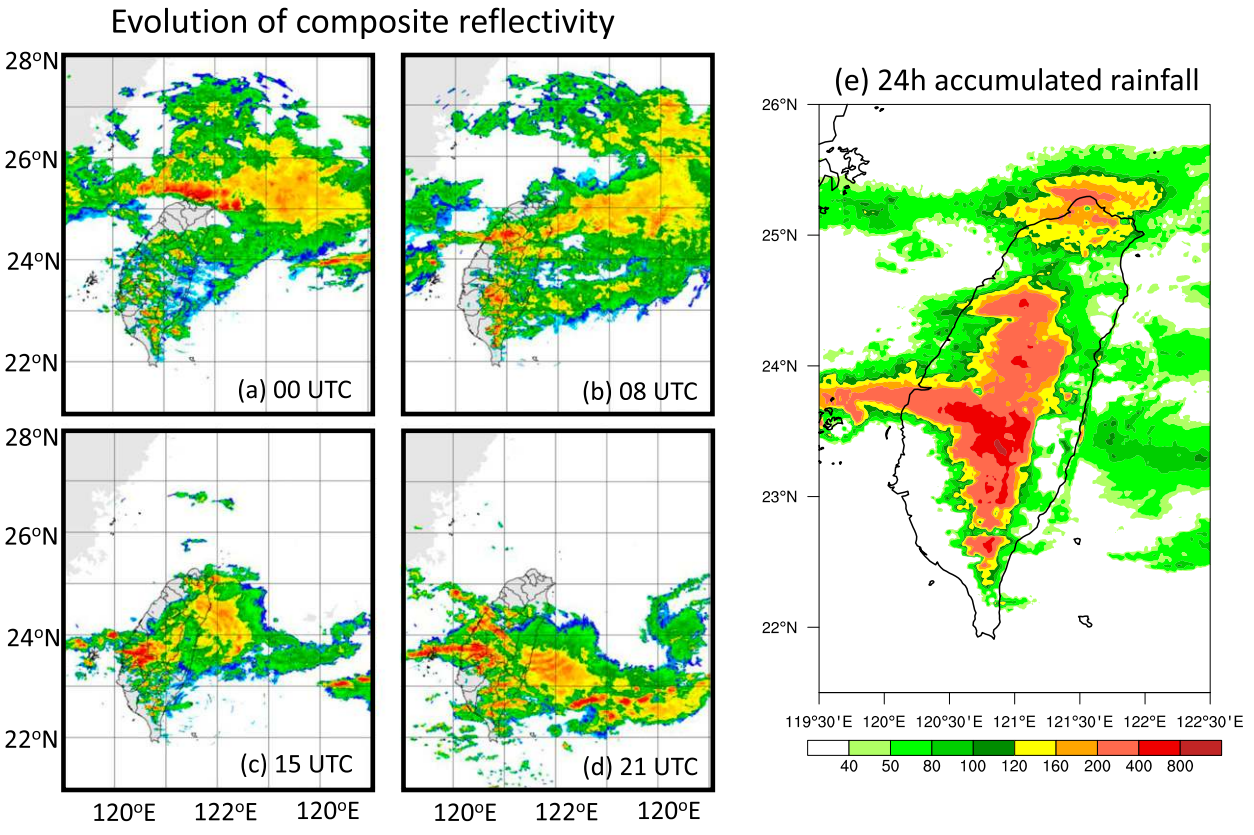

FIG. 1. Radar composite reflectivity at (a) 0000, (b) 0800, (c) 1500, and (d) 2100 UTC 2 Jun 2017. (e) The 24-h accumulated rainfall between 0000 UTC 2 Jun and 0000 UTC 3 Jun 2017.

updated by $x_0^n = x_0^{n-1} + \delta x_0^n$ and the first guess trajectory $M_k(x_0^n)$ is produced for the next outer loop $n + 1$. The basic assumption of the incremental approach is that with enough number of outer loop iterations the solution of the cost function (4) can gradually approximate that of the nonlinear cost function (1).

To simplify the computation of $\mathbf{B}^{-1}$, the background error covariance matrix is decomposed by $\mathbf{B} = \mathbf{U}\mathbf{U}^{\mathrm{T}}$ and a control variable transform by $\delta x_0 = \mathbf{U}\mathbf{v}$ is applied where $\mathbf{v}$ is the vector of control variables to be minimized in the cost function (4). The control variables used in this study are u wind, v wind, temperature T, surface pressure Ps, pseudo–relative humidity, and cloud control variables of cloud water, rainwater, ice, and snow mixing ratios. The pseudo relative humidity is defined by the ratio between water vapor and its saturated value in the background. For the momentum control variables, Sun et al. (2016) demonstrated that u wind and v wind outperformed streamfunction and velocity potential for the high-resolution regional model application. The operator $\mathbf{U}$ is implemented through a recursive filter in the horizontal direction and an EOF (empirical orthogonal function) decomposition in the vertical direction.

The method for radar radial velocity and reflectivity data assimilation in WRFDA 3D-Var and 4D-Var has been described in several previous publications (Xiao et al. 2005, 2007; Wang et al. 2013a,b; Sun and Wang 2013; Sun et al. 2016) and the reader is referred to them for technical details. WRFDA has two options for radar reflectivity assimilation: one directly assimilates the reflectivity observations via an observation operator (Xiao et al. 2007) and the other indirectly assimilates the reflectivity via a microphysical retrieval (Wang et al. 2013a). The current study uses the indirect method. Wang et al. (2013a) showed that the linearization of the reflectivity forward operator, as required by the incremental formulation of the cost function, could result in a dry bias in rainwater analysis. Thus, they proposed to assimilate the derived hydrometeor mixing ratios whereby the forward operator in the cost function was avoided. The derivation of the hydrometeor mixing ratios, including rain, dry snow, wet snow, and hail, follows that introduced by Gao and Stensrud (2012).

The rainfall data assimilation in our study followed that described by Ban et al. (2017). As shown below, a forward operator is necessary to compute the model accumulated (from time step 1 to the end of the

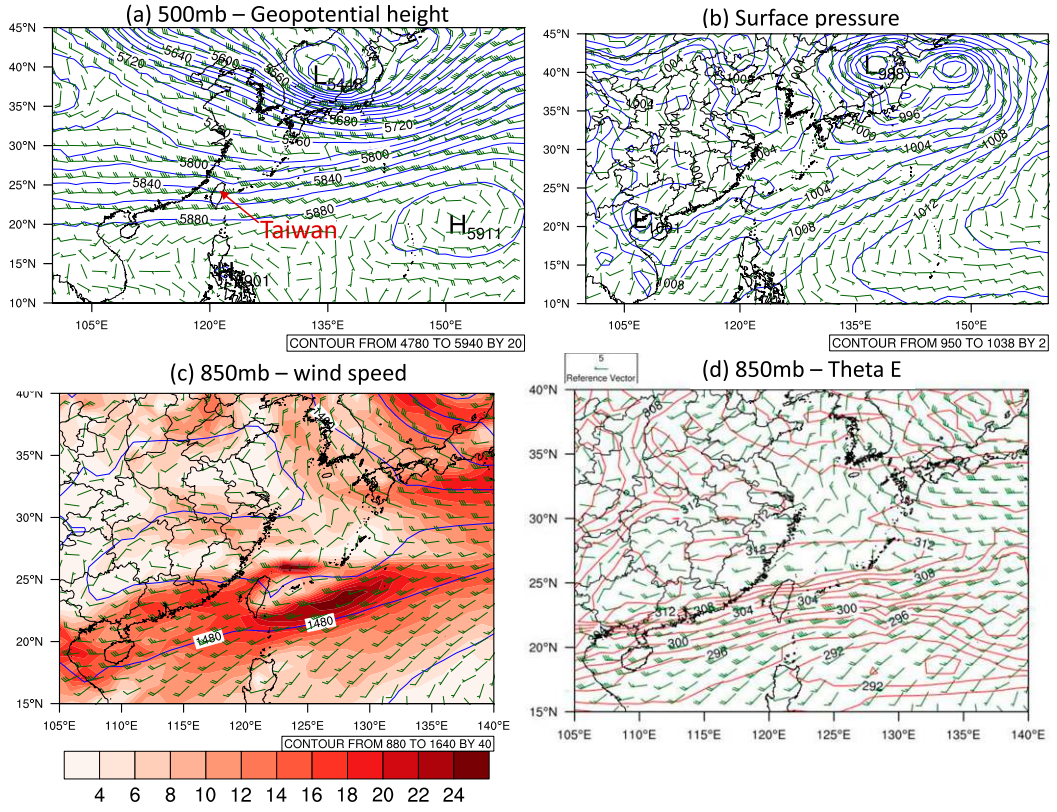

FIG. 2. Synoptic situation from GFS analysis valid at 0000 UTC 2 Jun 2017 as presented by (a) 500-mb geopotential height (contour) and wind vectors, (b) surface pressure (contour) and wind vectors, (c) 850-mb wind speed (color fill), geopotential height (contour) and wind vectors, and (d) 850-mb equivalent potential temperature (contour) and wind vectors.

assimilation window nt with the increment dt) rainfall from the forecast rainwater in order to obtain the difference between the modeled and observed rainfall:

$$J = J_b + J_o + \left(\sum_1^{nt} \frac{\rho_0 q_{r0} V_T \, dt}{\rho_w} \times 10^3 - \mathrm{RN}^{\mathrm{ob}}\right)^{\mathrm{T}} \times O_R^{-1} \left(\sum_1^{nt} \frac{\rho_0 q_{r0} V_T \, dt}{\rho_w} \times 10^3 - \mathrm{RN}^{\mathrm{ob}}\right), \quad (5)$$

where J_b is the background term [i.e., the first term in (4)] and J_o represents the observation term including all observations other than rainfall. $\mathrm{RN}^{\mathrm{ob}}$ stands for observed rainfall in mm accumulated over the 4D-Var assimilation window and O_R is the observation error covariance; their details will be described in the next section. The variables q_{r0} and ρ_0 are the rainwater mixing ratio and dry air density at the lowest model level and ρ_w is the liquid water density at the lowest model level. The rainfall terminal velocity V_T is given by

$$V_T = 36.34(0.001 \rho q_r)^{0.1346} \left(\frac{\rho_0}{\rho}\right)^{0.5}, \quad (6)$$

where q_r is the rainwater mixing ratio in $g\ g^{-1}$ and ρ is the dry air density. The sensitivity of the rainfall observation term with respect to the prognostic model variables at $t = 0$ is determined by the 4D-Var adjoint model.

The assimilations of both radar reflectivity and rainfall in WRFDA 4D-Var depend on a microphysical scheme to create multivariate correlation and impact on the dynamical and thermodynamical variables. There are two such schemes available in WRFDA 4D-Var along with their adjoints. One is a large-scale condensation scheme and the other is a warm-rain microphysical scheme described in Wang et al. (2013b). The latter is used in the current study. The WRF Model and its DA system configurations in the current study will be described in section 4.

3. The heavy rainfall case and observational data

a. *Description of the 2 June 2018 heavy rainfall event*

A convective rainband formed as a mei-yu frontal system reached the northern tip of Taiwan island at 0000 UTC 2 June and then propagated southward before 1500 UTC when its west segment became

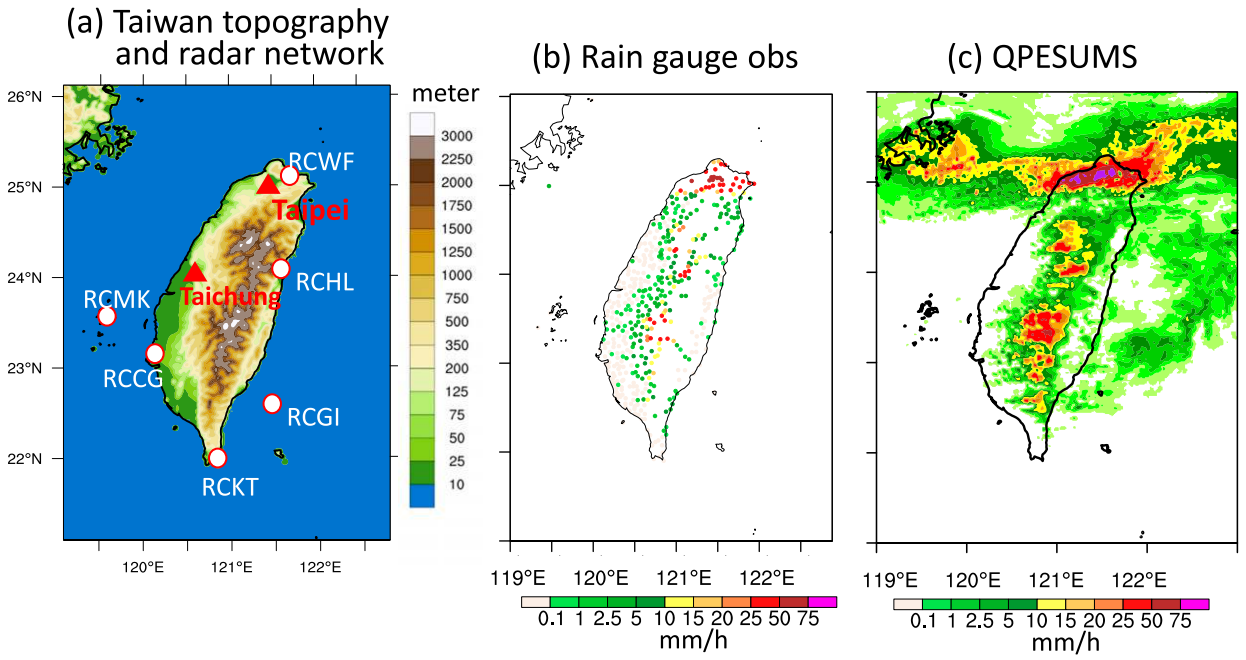

FIG. 3. (a) Taiwan topography, the locations of four S-band radars of RCWF, RCHL, RCKT, and RCCG and two C-band radars RCMK and RCGI, and the locations of Taipei and Taichung cities, around which the areas were mostly impacted by the 2 Jun 2017 heavy rainfall. (b) Observed hourly rainfall by Taiwan rain gauge network valid at 0000 UTC 2 Jun 2017. (c) As in (b), but from QPESUMS that combines radar QPE and rainfall from the gauge network.

stationary (Figs. 1a–d), producing large amount of accumulated rainfall in central Taiwan that reached more than 800 mm in 24 h (Fig. 1e). The 24-h accumulated rainfall clearly shows that Taipei and its vicinity, central west plains south of Taichung, and the central mountains were the major regions hit by the heavy rainfall (see Fig. 3a for the locations of these cities and Taiwan topography). The heaviest hourly rainfall was recorded at 108 mm by a station in central Taiwan. The heavy rainfall system caused major floods and mudslides in northern and central areas of Taiwan, and cancellation of hundreds of flights and close of Taipei Songshan Airport for several hours.

The mei-yu system formed as a low pressure system in northeastern Asia, shown in Fig. 2a, deepened on 1 June 2017. Coupled with a subtropical high located in the Pacific Ocean, it created a large pressure gradient and strong wind jet in eastern Asia. A low-level southwesterly jet swiped over Taiwan (Figs. 2b,c), bringing moisture to Taiwan. The high moisture along with the cold air from the north resulted in a region of large gradient of equivalent potential temperature across Taiwan with a southwest to northeast orientation (Fig. 2d). This synoptic situation agrees well with those typical for mei-yu rainbands that occurred in Taiwan (Chen and Yu 1988).

Although our ability in predicting the large-scale mei-yu rainband has improved over the years with improved global model resolution and data assimilation, the challenge remains in accurately forecasting the embedded heavy rainfall that is often closely associated with local mesoscale circulations and topographical forcing (Chen 2004). By assimilating local observations such as those from radar network and surface rainfall network we anticipate that the model's skill in short-term heavy rainfall prediction can be improved.

b. *Description of radar and rainfall data*

Radar radial velocity and reflectivity observations used in this study were collected by Taiwan's operational radar network that included four S-band and two C-band Doppler radars, whose locations are shown in Fig. 3a. These six radars routinely produce radial velocity and reflectivity volumetric observations with the same update rate of 7 min but different number of elevation angles. With reflectivity observations from this radar network, an integrated operational hourly rainfall product, named Quantitative Precipitation Estimation and Segregation Using Multiple Sensors (QPESUMS; Zhang et al. 2008), are produced. In QPESUMS, an empirical Z–R (reflectivity–rainfall) relation is first used to produce a gridded hourly rainfall field updated every 10 min with a 1 km horizontal resolution and then the rainfall field is integrated with rainfall measurements from Taiwan's surface rain gauge network (see Fig. 3b)

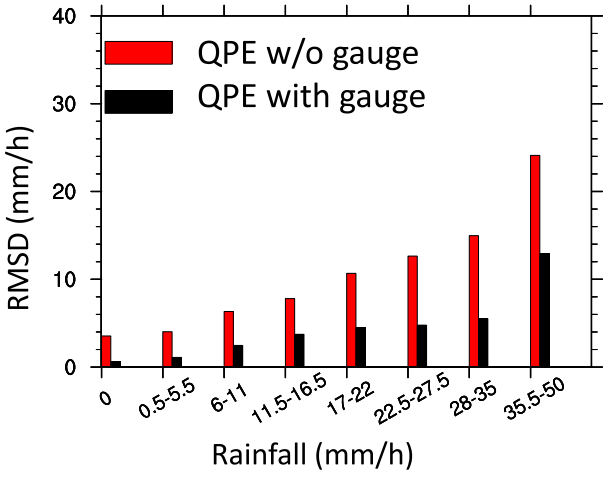

FIG. 4. Root-mean-square difference (RMSD) between hourly rainfall from Taiwan rain gauge network and radar QPE computed at the points of the rain gauge stations. The ref and black bars represents the RMSD using radar QPE before and after (QPESUMS) the rain gauge adjustment by an algorithm that produced QPESUMS rainfall.

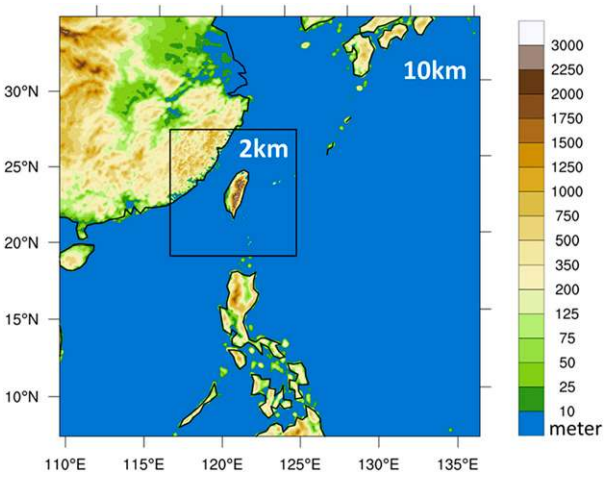

FIG. 5. Nested WRF forecast model domain for all experiments listed in Table 1. The radar and rainfall data assimilation, either alone or combined, is conducted on the 2-km domain while the GTS data assimilation in CTRL_3D is conducted on both domains.

using a local bias correction method. The final QPESUMS product valid at 0000 UTC 2 June 2017 is shown in Fig. 3c.

Comparing Fig. 3c with Fig. 3b, it is apparent that the integrated QPESUMS rainfall product has a higher spatial resolution and coverage than the rain gauge network. When assimilating radar and rainfall data simultaneously, one important factor that can impact the effectiveness of the assimilation is their relative information content. The total observation number from the 513 rain gauge stations is 513 at a given time, which is about three orders smaller in comparison with the total data number of a typical gridded 3D radar volumetric dataset. With a 1 km resolution, the gridded QPESUMS rainfall product results in the number of data points having the same order as that of radar reflectivity data at a single time. This is one of the reasons why we chose to assimilate the integrated rainfall product QPESUMS in this study rather than assimilating the rain gauge data directly. Although not directly assimilated, the rain gauge observations play a critical role in correcting the inevitable bias in the raw radar QPE. Figure 4 shows the RMS difference between rain gauge and radar QPE with and without the gauge correction computed with hourly rainfall data between 2 and 4 June 2017.

Because the QPESUMS rainfall is derived from radar reflectivity, a natural question is whether its correlation with the reflectivity will cause negative impact if both are assimilated. We will show an experiment in section 5 designed to answer this question.

For radar data quality control, the automated radar data preprocessing and quality control module embedded in NCAR's Variational Doppler Radar Analysis System (VDRAS; Sun and Crook 1997) was used to produce gridded PPI data with a 2 km horizontal resolution. The module includes several quality control algorithms to deal with ground clutters and aliased velocities and to perform random noise filtering, superobbing, and error estimate. Some of the algorithms were described in Sun (2005) and Lim and Sun (2010).

A rainfall data quality control procedure is contained in the QPESUMS algorithm to remove rainfall data with large deviation between the rain gauge and radar derived QPE. Based on Fig. 4, a constant error of 3 mm h^{-1} (e.g., 1 mm for the 20-min accumulation in our experiments) is specified for the QPESUMS rainfall data assimilation.

4. Model and DA configurations and experimental design

We used WRFDA 3.9.1 and WRF 3.9.1 for the current study. The experimental domain is shown in Fig. 5 with a 10/2 km nest and 51 vertical levels. The initial conditions at the cold-start time (0000 UTC 2 June 2017) and boundary conditions were provided by GFS 0.25° analysis., The radar and rainfall data were assimilated only in the 2 km domain because of their availability in this domain. A baseline experiment (CTRL_3D; red highlight in Fig. 6) with 3-hourly cycled WRFDA 3D-Var assimilating conventional Global Transmission System (GTS) observations on both domains was initialized at 0000 UTC 2 June 2017 by GFS analysis and provided first guess for the 4D-Var experiments. The background error statistics for both domains were obtained from the

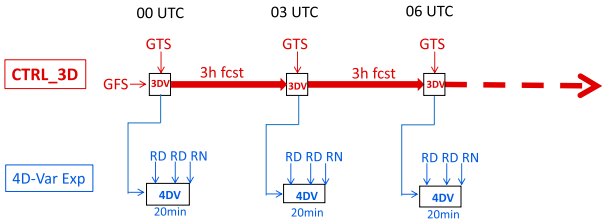

FIG. 6. Schematic diagram of data assimilation strategies for CTRL_3D (red) and all the 4D-Var experiments (blue). GFS: Global Forecast System; GTS: global transmission system; 3DV: 3D-Var; 4DV: 4D-Var; RD: radar; RN: rainfall.

Central Weather Bureau of Taiwan (CWB), which are used in their operational 10/2-km DA and forecast system. The statistics was generated by subtracting 12-h forecast from 24-h forecast valid at the same time initialized every 12-h from downscaled GFS analysis for the month of July 2017.

Four 4D-Var experiments along with CTRL_3D are summarized in Table 1. The experiments Rn_4D, RvRf_4D, RvRn_4D, and RvRfRn_4D assimilate, respectively, QPESUMS rainfall data alone, radar radial velocity and reflectivity, radar radial velocity and QPESUMS rainfall, and all three observation fields. The experiments Rn_4D and RvRf_4D were conducted to compare the relative impacts of assimilating rainfall alone to assimilating radar alone. RvRfRn_4D evaluates the benefit of assimilating these two datasets simultaneously. RvRn_4D was designed to answer the question, by comparing it with RvRfRn_4D, whether the reflectivity data add any benefit or harm when rainfall data are already assimilated due to the possible correlation of these two datasets.

The configuration of the 4D-Var experiments is illustrated in Fig. 6 (blue highlight). All the 4D-Var experiments start from CTRL_3D analysis. The two-pass radar DA strategy assimilating the conventional data and radar data in two steps follows that of Tong et al. (2016). They demonstrated that assimilating radar observations separately from GTS data with a smaller length scale allowed better fit to radar data and resulted in improved convective forecasting. In this study the length scale in the 4D-Var experiments is reduced by half from the statistically computed BE used in CTRL_3D.

The initialization times are at 0300, 0600, 0900, 1200, 1500, 1800, and 2100 UTC. The assimilation window is 20 min in which there are two radar scanning volumes available from each radar. The short window is necessary to capture dynamical processes of convection essential for heavy rainfall (Wang et al. 2013b). The 20-min rainfall accumulation within the assimilation window is assimilated at the end of the window. Because the QPESUMS rainfall is hourly accumulation, the 20-min accumulated rainfall is estimated simply by dividing the hourly rainfall valid at the same time by three. Experiments were conducted (but not shown) to examine the sensitivity of DA to the 20-min rainfall estimated using different hourly rainfall rates (available every 10 min) that overlap the assimilation window and their results showed little differences. All of the 4D-Var experiments were run with three outer loops updating the nonlinear basic state and 25 iterations for each outer loop to minimize the cost function.

After the data assimilation at the multiple of 3 h from 0300 to 2100 UTC, 6-h forecasts were run for all of the five experiments. The physics options used in the WRF forecast model include the Thompson bulk microphysics scheme, the Mellor–Yamada–Janjić (MYJ) PBL scheme, the Monin–Obukhov surface layer scheme, the RRTMG radiation scheme, and the Kain–Fritsch cumulus parameterization scheme that is applied only in the outer domain. The description of the above schemes can be found in the WRF-ARW technical report (Skamarock et al. 2008).

5. Results

a. *Results from single observation tests*

We first conducted single observation tests for the 4D-Var experiments Rn_4D, RvRf_4D, RvRn_4D, and RvRfRn_4D to compare their multivariate responses of analysis increments to different observation inputs given at a single grid point. The background of these single observation tests is the 3-h WRF forecast from the experiment CTRL_3D valid at 0600 UTC 2 June 2017. The location of the single observation was carefully chosen such that both the background and the observations produced precipitations. The single observations of radial velocity and reflectivity were taken from the nearest

TABLE 1. Summary of experiments.

Exp	Rainfall	Radial velocity	Reflectivity	DA method	Single OBS test
CTR_3D	No	No	No	3D-Var	No
Rn_4D	Yes	No	No	4D-Var	Yes
RvRf_4D	No	Yes	Yes	4D-Var	Yes
RvRn_4D	Yes	Yes	No	4D-Var	Yes
RvRfRn-4D	Yes	Yes	Yes	4D-Var	Yes

TABLE 2. Single observation and background values.

	Radial velocity	Reflectivity	Rainfall
Background	16.87 m s^{-1}	7.64 dBZ	0.12 mm
Observation	19.9 m s^{-1}	36 dBZ	5.8 mm

radar at the height of 1500 m and the 20-min rainfall was taken from QPESUMS. Table 2 summarizes the background and observation values for reflectivity, radial velocity, and rainfall.

Figures 7–9 show the analysis increments (from forecast background) of v-wind, temperature, and water vapor mixing ratio, respectively, from the four single observation experiments. For the wind increments, the results in Fig. 7 suggest that radar DA (Fig. 7a) plays a much more significant role than rainfall DA (Fig. 7b). Comparing RvRf_4D with an experiment assimilating the reflectivity observation alone (not shown) suggested that the increment contribution was dominantly made by the radial velocity, which is also evidenced by the close resemblance between the wind increments of RvRn_4D (Fig. 7c) and RvRfRn_4D (Fig. 7d).

In contrast to the wind increments, the temperature (Fig. 8) and humidity (Fig. 9) increments both show larger responses to rainfall data in comparison with radar data. Their combined assimilation with (Figs. 8d, 9d)

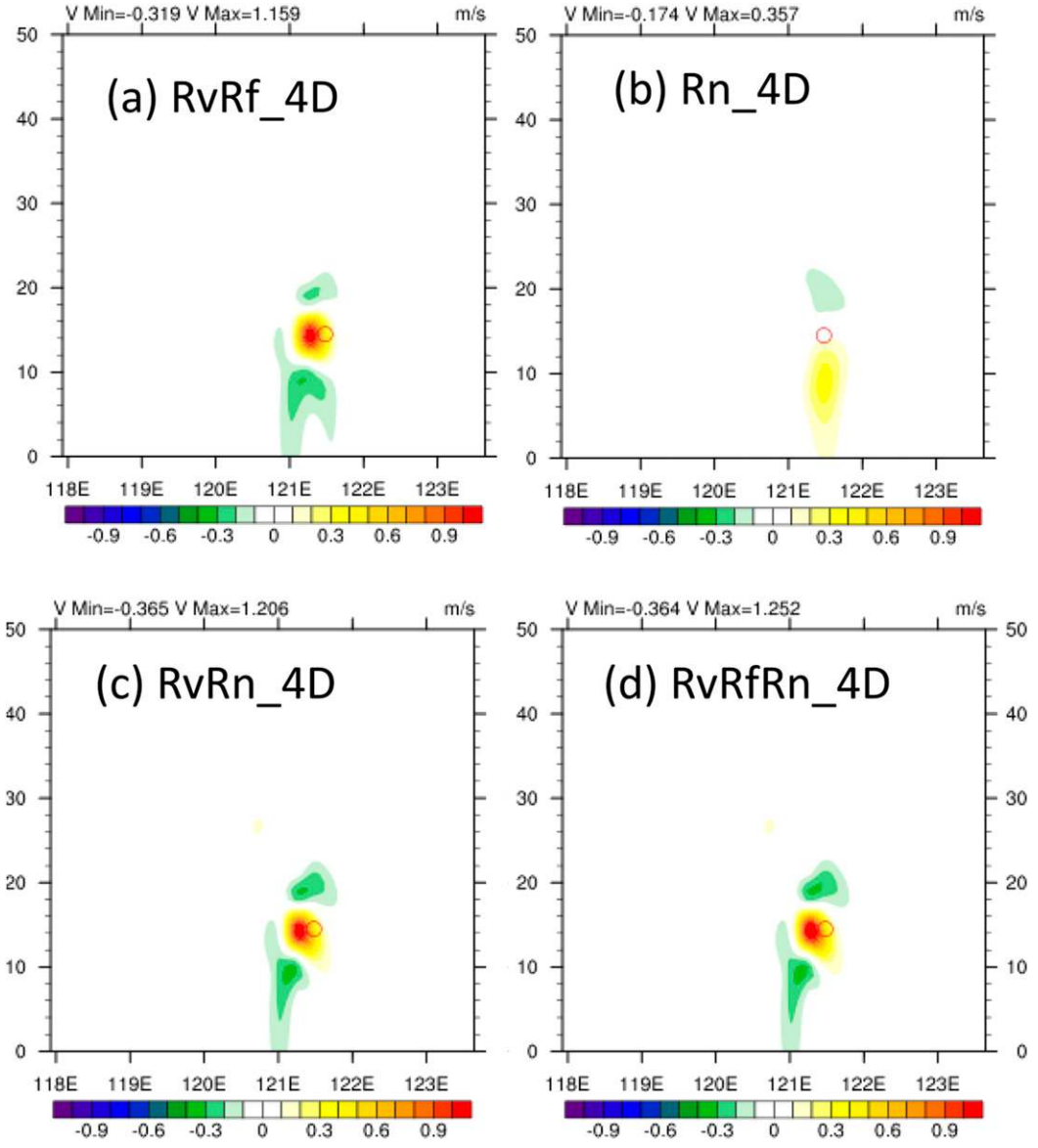

FIG. 7. V-wind increment on a west–east vertical plane across the single observation point from the four single observation tests: (a) RvRf_4D, (b) Rn_4D, (c) RbRn_4D, and (d) RvRfRn_4D.

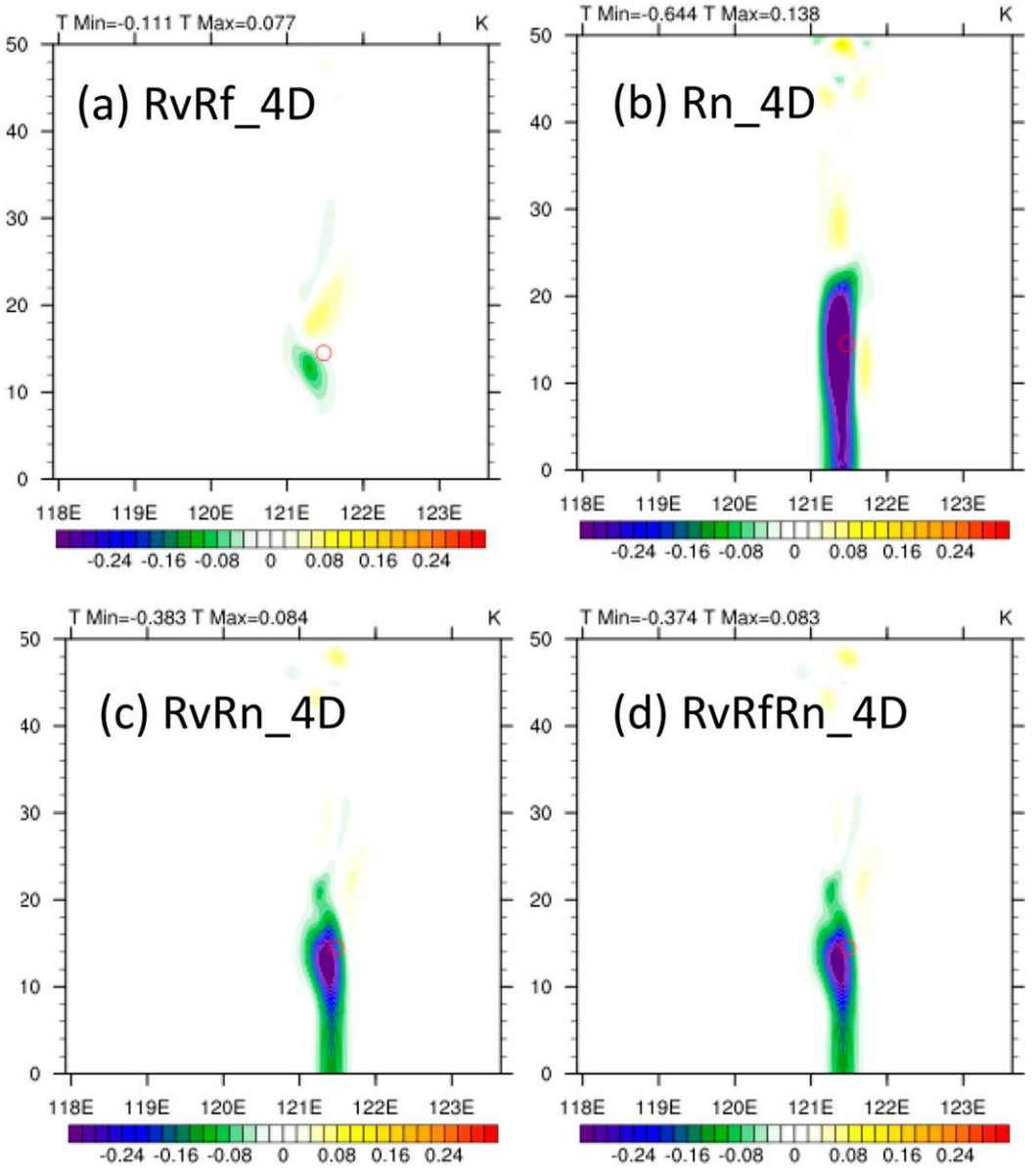

FIG. 8. As in Fig. 7, but for temperature.

or without (Figs. 8c, 9c) the reflectivity reduces the increments for temperature and humidity. The greater temperature and humidity responses produced by the rainfall DA are not surprising because the accumulated rainfall on the ground at the end of the assimilation window must correspond to sufficient precipitable water in the column of air above at the initial time (positive humidity increments) or cooled column of air above the surface rainfall (negative temperature increments). Note that the vertical distribution of the humidity and temperature increments are mainly determined through the adjoint of the microphysical processes in the 4D-Var within the 20-min window.

Although the assimilation of the two-dimensional accumulated rainfall exhibits larger effect in the analysis in comparison with the assimilation of the three-dimensional instantaneous field of reflectivity, we will show later in this section in the data assimilation experiments that the large multivariate increments generated by the rainfall DA can be prone to error without the dynamical constraint provided by radar observations, especially those of radial velocity.

b. Results from the 2 June 2017 mei-yu case study

When assimilating different types of observations simultaneously in a variational framework, a basic check

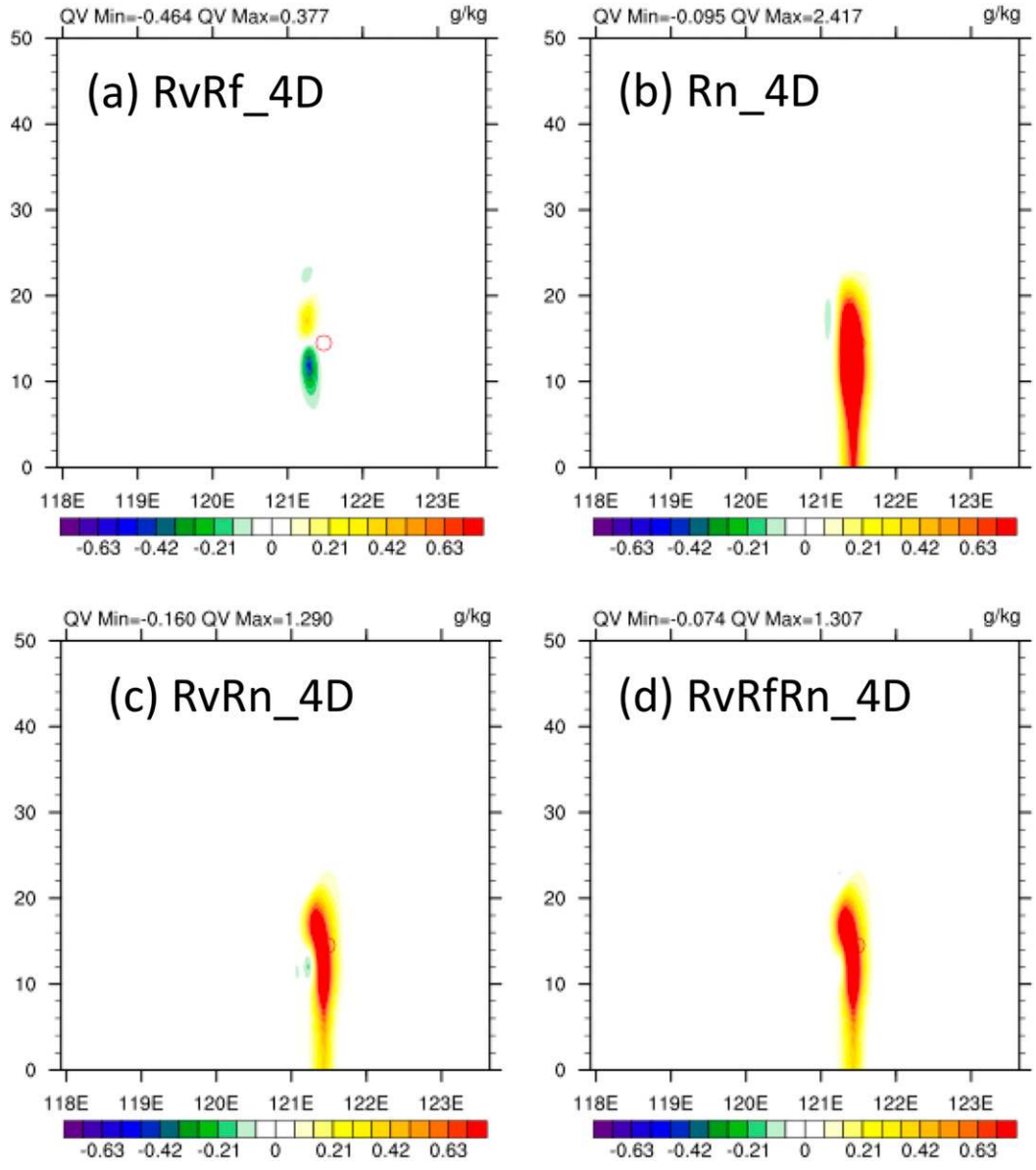

FIG. 9. As in Fig. 7, but for water vapor mixing ratio.

to determine whether the assimilation behaves properly is by examining the convergence of the minimization of the cost function. Figure 10 shows the cost function reduction with respect to minimization iteration (accumulated with the three outer loops) for the three experiments Rn_4D, RvRf_4D, and RvRfRn_4D. The cost function of RvRn_4D is not shown because it is similar to that of RvRfRn_4D. As expected, jumps occur at the accumulated iterations 25, 50, and 75 because of the mismatch between the linearized state (for the inner loop minimization in the incremental 4D-Var) and the nonlinear state when the nonlinear basic state is updated. The cost functions in the three experiments are all reduced effectively within each outer loop although their absolute magnitudes are quite different. To compare the relative reductions of the cost functions among the three experiments, we plot the three cost functions normalized by their respective values at the first iteration in Fig. 10d. It is shown that the cost function from Rn_4D is reduced most rapidly among the three experiments. However, as will be shown later, the rapid reduction of the cost function fails to produce better analysis and forecasts, likely due to overfitting to the rainfall data without being constrained by the dynamical information from the radar radial velocity. From Fig. 10d, we also note that the large jump at the

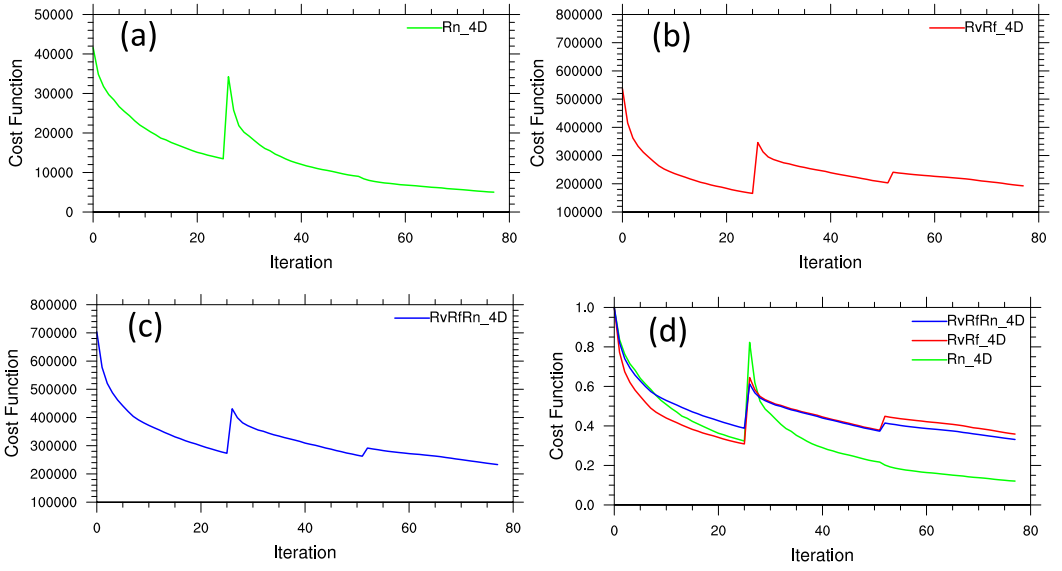

FIG. 10. Reduction of cost function with respect to number of iterations accumulated in three outer loops for (a) Rn_4D, (b) RvRf_4D, and (c) RvRfRn_4D at the analysis time 1500 UTC 2 Jun 2017. (d) The cost functions of the three experiments normalized by their respective first iteration values.

transition between the first outer loop and the second outer loop is much reduced when the rainfall data are simultaneously assimilated with the radar data.

To examine the impact of the combined assimilation of radar and rainfall data on heavy rainfall prediction, we first compare the skills of precipitation forecasts from the five experiments and then compare the differences of the analysis fields in wind, humidity and temperature in order to gain insight on the physical causes of the improved skill. The fractions skill score (FSS) of 6-h accumulated rainfall with a radius of influence of 10 km is computed against QPESUMS over the land for the five experiments and the result is displayed in Fig. 11, in which Figs. 11b–i show the scores of the forecasts initialized at each of the seven initialization times and Fig. 11a shows the average score over the seven forecasts. Note that larger radius sizes have also been tested for the FSS computation and found that the relative skills among the experiments do not change although the larger size increases the scores of all experiments.

From Fig. 11a we first note that the 4D-Var assimilation of radar and rainfall data, alone or combined, improves the precipitation skill over the control experiment (CTRL_3D) and the radar data experiment shows greater improvement (RvRf_4D) than the rainfall data experiment (Rn_4D). The most remarkable improvement is produced by RvRfRn_4D when both data sources are assimilated simultaneously with evidently higher scores than that of either Rn_4D or RvRf_4D.

From the single observation tests shown earlier, we noted that the impact of reflectivity on wind increments was much smaller than that of radial velocity and its impacts on temperature and humidity were insignificant in comparison with those from rainfall data assimilation. Comparing the precipitation skills between RvRn_4D (excluding reflectivity) and RvRfRn_4D in Fig. 11a, we see additional evidence that the contribution of the reflectivity to the precipitation forecasts is small although slightly positive. It is worth noting that the reflectivity data assimilation has been shown to result in notable impact in several of previous studies with 3D-Var (e.g., Xiao et al. 2007; Wang et al. 2013b; Weygandt et al. 2008), but the impact was indirectly produced by adjusting the dynamical fields of moisture or temperature based on an assumption of in-cloud saturation or latent heat release. Without the dynamical adjustment the hydrometeor mixing ratios could just fall to the ground after a few time steps into free model forecasts. The insignificant difference of precipitation forecast skills between RvRn_4D and RvRfRn_4D indicates that even with the 4D-Var technique with a microphysical scheme it is still difficult to fit the model to the reflectivity observations. One of the reasons can be that the 7-min update frequency of the radar volumetric data are not quick enough to capture the rapid development of microphysical variables in moist convection. Fabry and Sun (2010) demonstrated that the error growth in rainwater mixing ratio reached a nonlinearity threshold in less than 10 min in contrast to 70 min for velocity, meaning that it is much more difficult to fit the model to reflectivity than to radial velocity even with the short 20-min assimilation window used in this study. We are

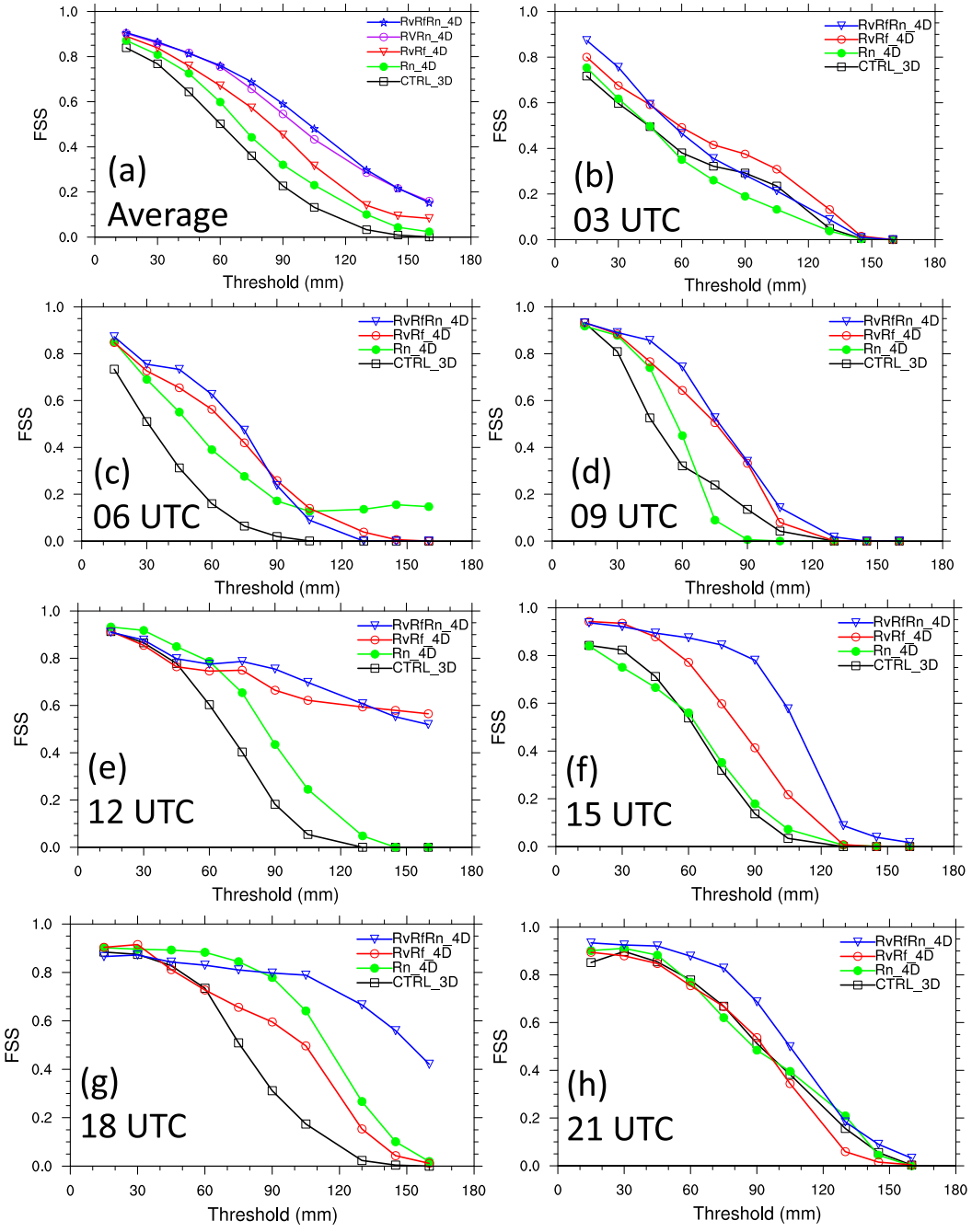

FIG. 11. Fractions skill scores (FSS) of 6-h accumulated rainfall forecasts, initialized at (b) 0300, (c) 0600, (d) 0900, (e) 1200, (f) 1500, (g) 1800, and (h) 2100 UTC, respectively, with respect to rainfall amount for the four experiments CTRL_3D, Rn_4D, RvRf_4D, and RvRfRn_4D. (a) The FSSs averaged over the seven forecasts for the four experiments plus RvRn_4D.

currently investigating a multiple-time-window scheme in which the reflectivity assimilation is done with a smaller window length than that of the radial velocity and the result will be reported in a separate paper.

The FSSs of the 6-h rainfall forecasts initialized at different times are shown in Figs. 11b–h (note that RvRn_4D is not included in these figures because it differs little from RvRfRn_4D as shown in Fig. 11a). We first notice that the impact of Rn_4D on the rainfall forecast skill varies at different initialization times: negative impacts at higher thresholds for the 0300 and 0900 UTC forecasts but significantly positive impacts at

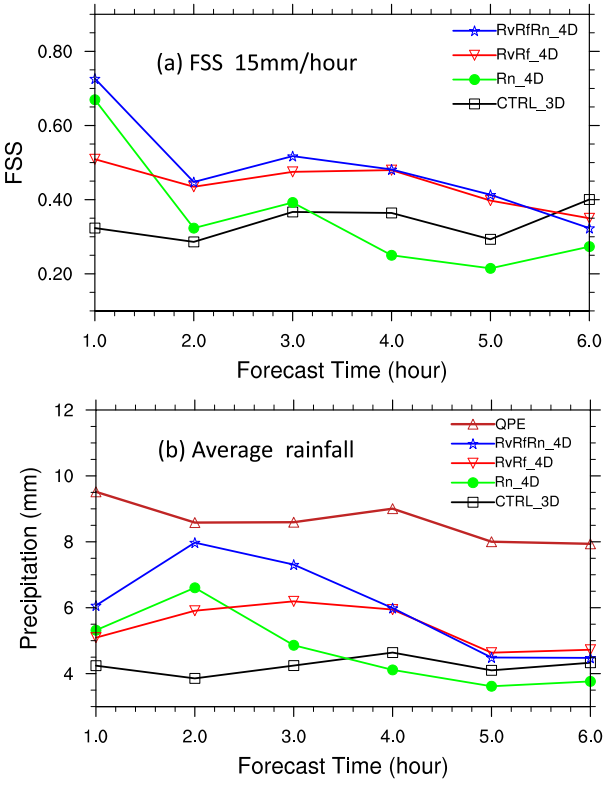

FIG. 12. (a) FSSs of hourly rainfall forecasts with respect to forecast hour for the threshold of 15 mm, averaged over seven forecasts, for CTRL_3D, Rn_4D, RvRf_4D, and RvRfRn_4D. (b) As in (a), but for rainfall averaged over all grid points on land.

0600, 1200, and 1800 UTC. In contrast, the radar data assimilation produced significant positive impacts for all forecasts except for higher thresholds at 2100 UTC. The combined assimilation improves the rainfall forecast skill over the two individual assimilation experiments for most forecast runs with significant improvement at 1500, 1800, and 2100 UTC.

We further examine the FSSs of hourly precipitation forecasts from the above experiments (except for RvRn_4D) to see how their skills vary with time (Fig. 12a). The experiment Rn_4D significantly improves the skill of hourly rainfall forecast in the first hour and then its skill decreases with time and becomes lower than that of the control experiment after the third hour. Compared with the rainfall DA, the radar DA results in larger improvement over CTRL_3D on the precipitation skill except for the first hour and the last hour. Combining the two data sources enhances the skill from the two individual assimilation experiments for most of the forecast hours.

The average rainfall over the land (Fig. 12b) indicates that all the forecasts from the four DA experiments underpredict the rainfall amount. That is not surprising given the extremely heavy rainfall amount observed. The individual assimilation experiments Rn_4D and RvRf_4D improve the forecasts of the rainfall amount over the control experiment in the first 3 h and in the entire 6 h, respectively. As both radar and rainfall data are assimilated in RvRfRn_4D, further improvement is resulted in the first 3 h over both the radar-only experiment and the rainfall-only experiment. Also, the combined assimilation results in large improvement over the rainfall-only experiment in the entire 6 h.

By comparing the 6-h precipitation patterns, we found that the combined assimilation of rainfall and radar data results in improved forecasts of location, intensity, or both for the forecast runs at most of the initialization times. Figures 13 and 14 provide two examples of rainfall forecasts initialized, respectively, at 0600 UTC when the rainband propagated southward and at 1500 UTC when it was stalled by the strong southwesterly flow. At 0600 UTC, the control experiment successfully forecasts the propagating rainband in northern Taiwan but the location is to the north of the observed rainband (indicated by the blue oval) and further it misses most of the rainfall on the mountains of central Taiwan (the black circle). Both the radar or rainfall data assimilation experiments result in some degree of improvement in these two areas but the experiments RvRfRn_4D shows the most significant improvement. It not only successfully forecasts the location of the main rainband but also substantially improves the rainfall forecast on the mountains of central and southern Taiwan in terms of area coverage as well as intensity. For the 1500 UTC (Fig. 14) forecasts, the control experiment underpredicts the rainfall amount and again the rainfall area is to the north of the observed. While both RvRf_4D and RvRfRn_4D improve the location, orientation, and intensity of the rainband, the latter shows substantial improvement on intensity.

To see how the different data assimilation experiments modify the initial conditions, we compare the analysis increments (from CTRL_3D background) in Fig. 15 among the experiments Rn_4D, RvRf_4D, and RvRfRn_4D for the *y*-component wind, temperature, and humidity fields on the eighth model level (~930 mb) at the analysis time 1500 UTC. For the wind field, both the rainfall and radar data produce large increments (Figs. 15a,b). However, the radar data has larger impact than rainfall data in the combined assimilation (Fig. 15c) as suggested by the similarity between RvRf_4D and RvRfRn_4D. Interestingly, the large increments on the sea west and east of the island in the rainfall-only experiment (Fig. 15a) are suppressed when radar data are also assimilated in RvRfRn_4D. For the humidity analysis, the rainfall-only experiment results in large increments in the areas of heavy precipitation (Fig. 15d) and

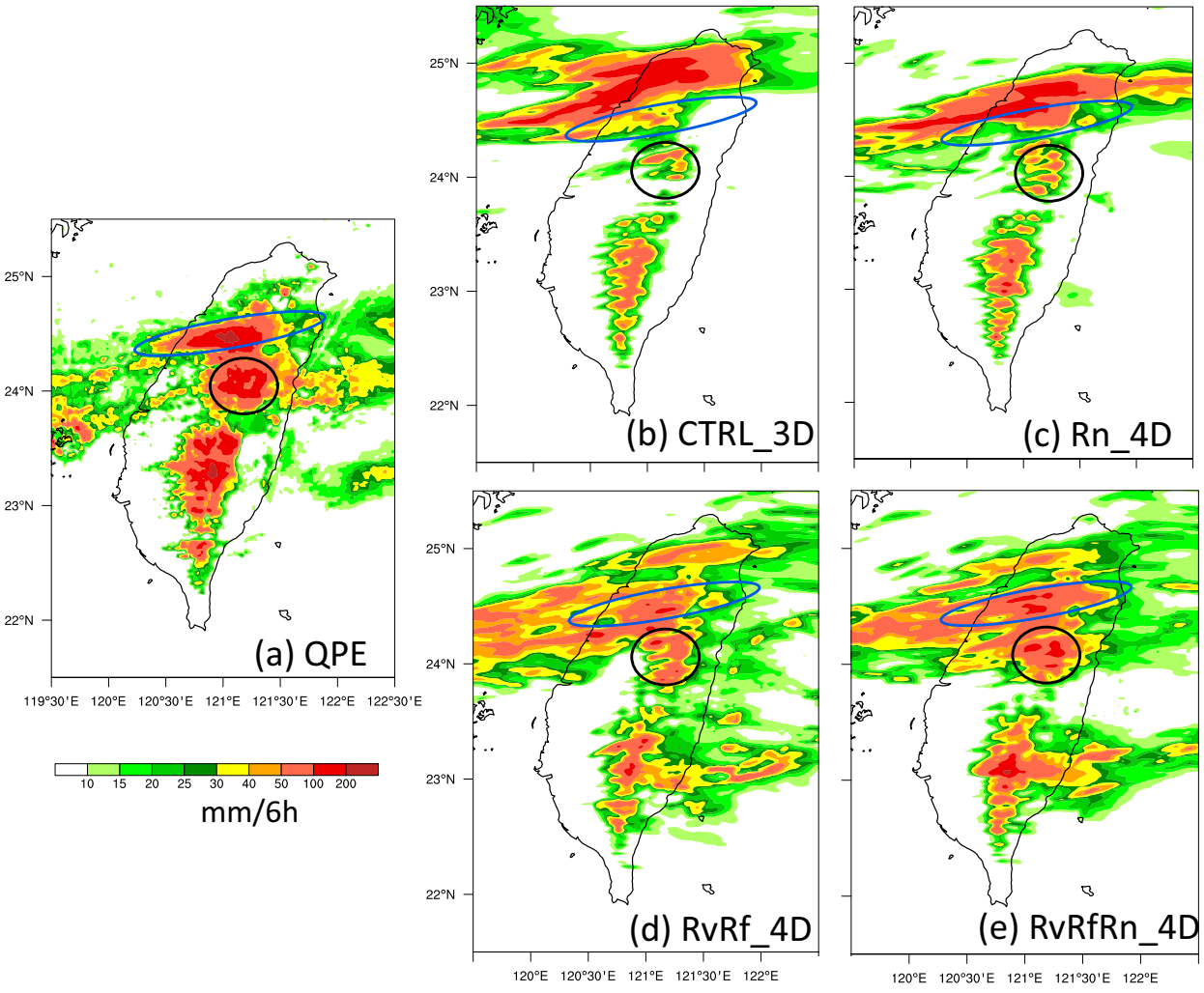

FIG. 13. Comparison of 6-h accumulated rainfall forecasts from the experiments (b) CTRL_3D, (c) Rn_4D, (d) RvRf_4D, and (e) RnRfRn_4D initialized at 0600 UTC 2 Jun 2017. (a) Rainfall from QPESUMS is shown in for verification.

they are substantially tuned down when radar data are simultaneously assimilated (Fig. 15f). Similarly to the humidity increments, the temperature increment in RvRfRn_4D largely follow the pattern of Rn_4D; nevertheless, the large negative increments in the center of the heavy rainfall band from Rn_4D, an indication of rapid precipitation fallout due to the lack of dynamical support, is much reduced.

The above comparison suggests that, similar to the single observation tests, the radar observations provide important information about the wind circulation in and around the precipitation area while the rainfall observations produce large convective-scale responses in the humidity and temperature fields. The combination of the two types of observations result in moderate increments of wind, humidity, and temperature fields because of the mutual constraining of the two data types.

To further understand what are the physical structures in the analysis fields that contribute to the improved precipitation forecasts when the two data sources are simultaneously assimilated, we show the relative humidity and wind vectors on the eighth model level for CTRL_3D, Rn_4D, RvRf_4D, and RvRfRn_4D in Fig. 16 at the initialization time 1500 UTC. We first notice that Rn_4D (Fig. 16b) creates a large area of near-saturation humidity covering the central Taiwan and its nearby sea. However, the high humidity area is concentrated to the central west plain region in RvRfRn_4D (Fig. 16d) along with a northwesterly flow not present in CTRL_3D (Fig. 16a) and Rn_4D (Fig. 16b). This flow is also shown in RvRf_4D (Fig. 16c) in the same region, suggesting that it comes from radar DA; however, without the rainfall DA the rainband region is apparently too dry, even drier than CTRL_3D. These results suggest that the northwest flow as well as the

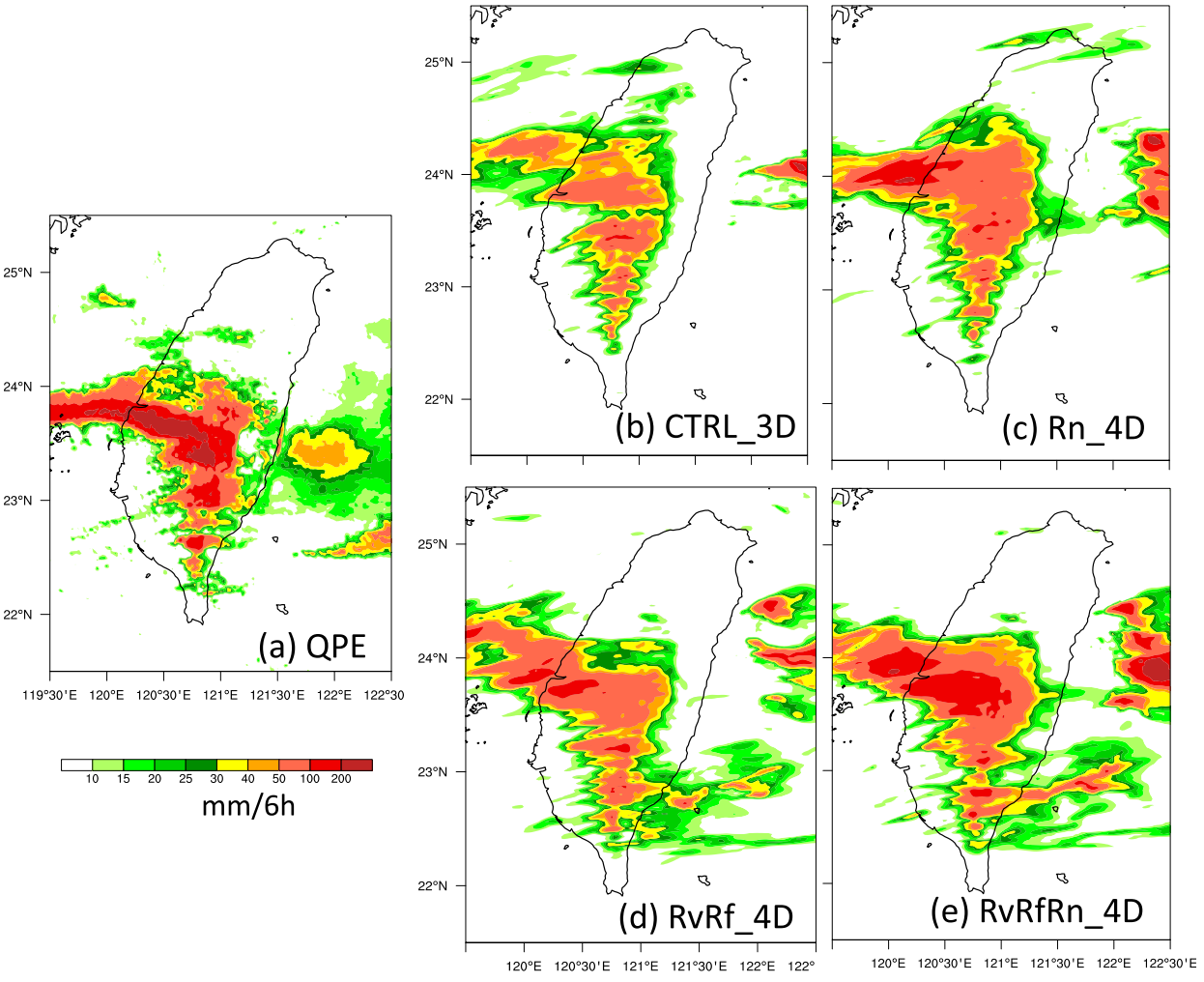

FIG. 14. As in Fig. 13, but for forecasts initialized at 1500 UTC 2 Jun 2017.

enhanced humidity are both responsible for enhancing the convective precipitation and hence improving the forecast skill. Without the enhanced humidity from the rainfall assimilation, the saturation of the updraft air column takes place during the forecast, which results in lower forecast skill as in RvRf_4D.

We then examine the vertical distribution of the humidity and wind fields in Fig. 17 in the cross section along A-B shown in Fig. 16a. While the background forecast from CTRL_3D (Fig. 17a) clearly exhibits a strong and deep updraft within the saturated columns around 40 km away from the point A, its location is not consistent with the observed rainband (see Fig. 14a). By assimilating radar data in RvRf_4D (Fig. 17c), a broad and deep updraft south of that in CTRL_3D is produced but the midlayer of the updraft columns are rather dry. On the other hand, although assimilating only rainfall data in Rn_4D (Fig. 17b) results in a successful suppression of the saturated humidity in the columns of the existing convection in the background field (around 40 km away from A in CTRL_3D) and the increase of humidity to the south of it, the experiment fails to produce updrafts essential for forecasting convection but instead downdrafts dominate in the moist region due to the water loading effect. The combined assimilation in RvRfRn_4D largely maintains the updraft structure in RvRf_4D while significantly enhancing the relative humidity with saturated air columns up to 9 km. The above comparison suggests that the combined assimilation results in an analysis with consistent dynamical (i.e., updraft) and thermodynamical (i.e., saturated air) features important for convective development. We believe it is this convective-scale consistency that results in the improved location and intensity forecasts of the rainband as demonstrated in Fig. 14. In Fig. 18, the relative humidity, wind, and rainwater mixing ratio fields at $t = 2$ h (valid at 1700 UTC) on the A-B cross section are compared. The combined assimilation (Fig. 18d) generates rainwater at

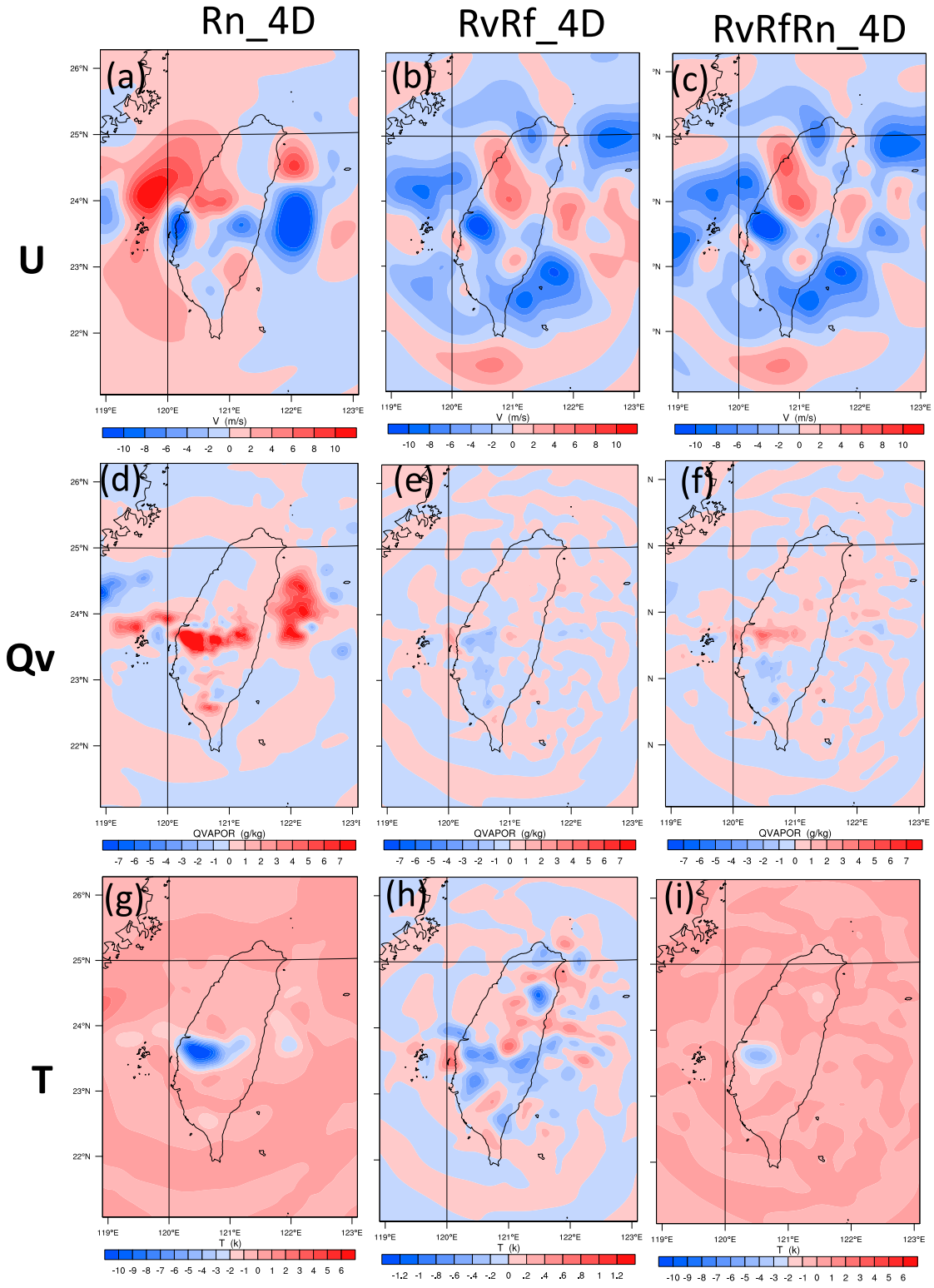

FIG. 15. Analysis increments of (a)–(c) *U* wind, (d)–(f) water vapor mixing ratio, and (g)–(i) temperature on the eight model level (~930 mb) from the experiments (a),(d),(g) Rn_4D, (b),(e),(h) RvRf_4D, and (c),(f),(i) RvRfRn_4D. Note that for the temperature increments the color scale in (h) is much smaller than that in (g) and (i).

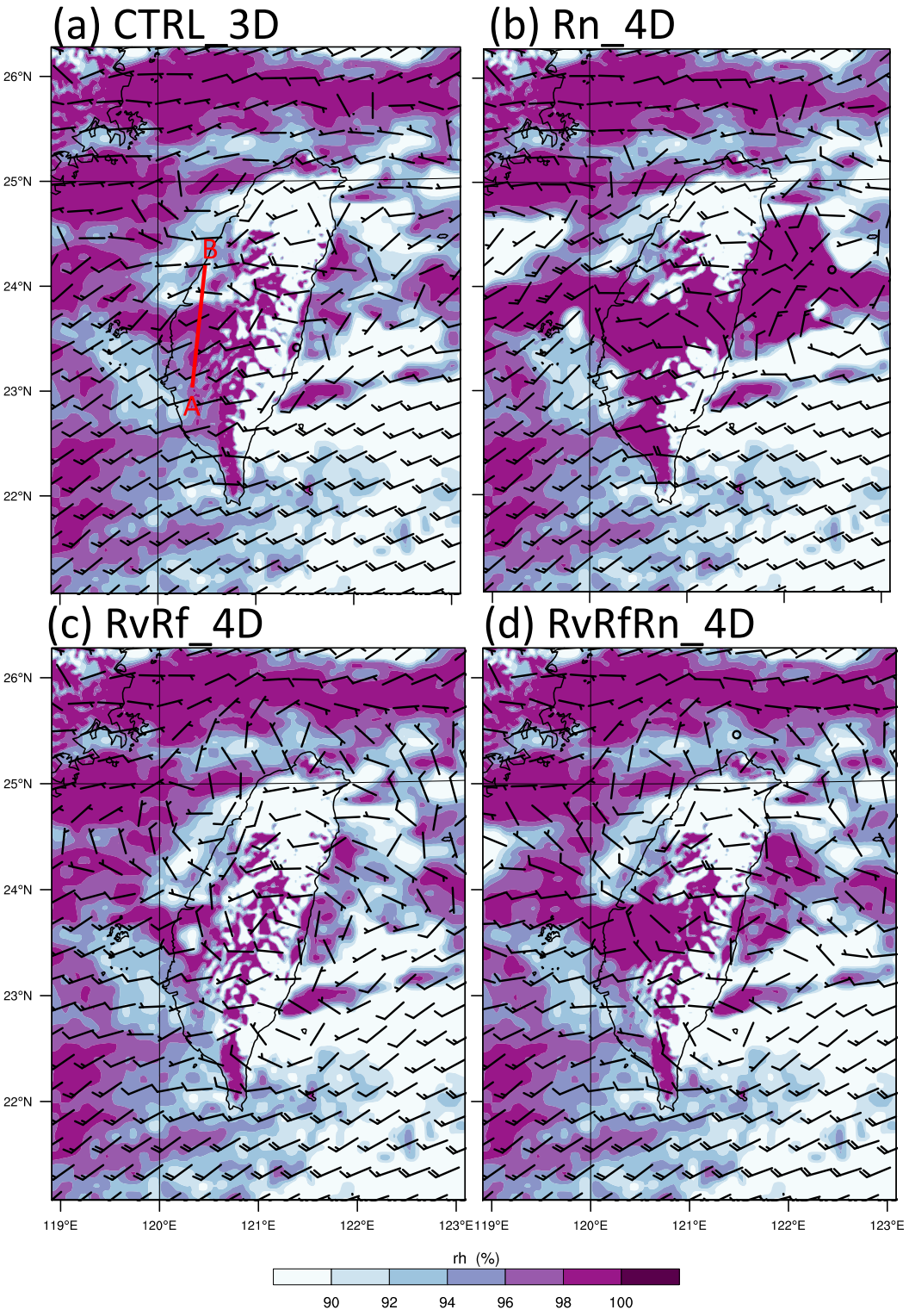

FIG. 16. Relative humidity analysis fields overlaid by wind barbs on the eighth model level at the 1500 UTC initialization time for (a) CTRL_3D, (b) Rn_4D, (c) RvRf_4D, and (d) RvRfRn_4D. The red line A–B indicates the cross-sectional location for Fig. 17.

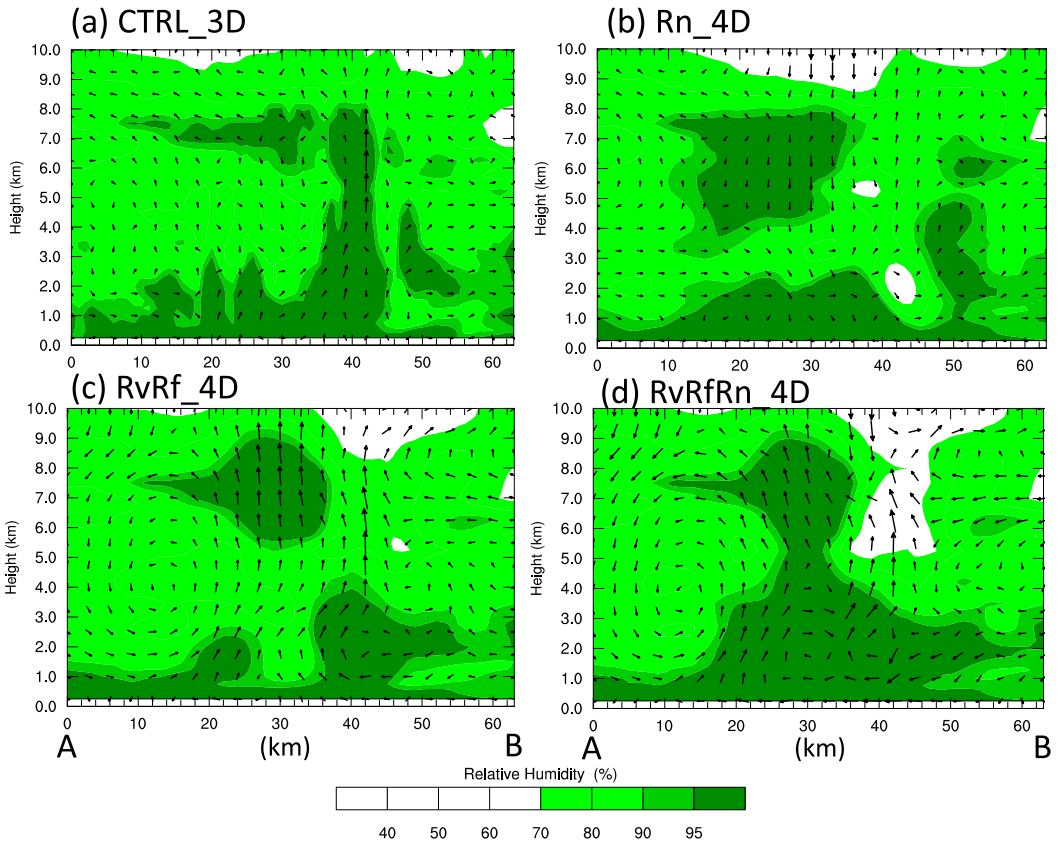

FIG. 17. Vertical cross section of relative humidity at the analysis time 1500 UTC along line A–B (illustrated in Fig. 16a) with wind vectors overlaid for the four experiments (a) CTRL_3D, (b) Rn_4D, (c) RvRf_4D, and (d) RvRfRn_4D.

about the right location of the observed rainfall maximum (indicated by the red arrow below the x axis) whereas the rainfall alone experiment (Fig. 18b) does not have any rainwater greater than $1\,g\,kg^{-1}$ likely because the dynamical spinup process causes a rapid rain-out in the first 2-h model integration. On the other hand, the radar DA experiment (Fig. 18c) produces rainwater around the location of the observed rainfall, but it is not as organized and high in magnitude as that in the combined assimilation experiment.

6. Summary and conclusions

In this study we assessed the benefit of simultaneous assimilation of radar and rainfall observations by conducting a number of 4D-Var experiments on a mei-yu heavy rainfall event that occurred in Taiwan on 2 June 2017. Four 4D-Var experiments Rn_4D, RvRf_4D, RvRfRn_4D, and RvRn_4D that, respectively, assimilate rainfall data, radar data including both radial velocity and reflectivity, rainfall and radar data, and rainfall and radar radial velocity were conducted and compared. A 3D-Var experiment CTRL_3D assimilating only conventional observations was used as the background and a baseline in the evaluation. The experiments RvRn_4D and RvRfRn_4D were compared to assess the additional contribution of radar reflectivity when rainfall data are assimilated. The three experiments Rn_4D, RvRf_4D, and RvRfRn_4D were compared to evaluate the benefit of combined rainfall and radar data assimilation on short-term heavy rainfall forecasts. The physical structures of the analysis fields from these three experiments were also compared to gain insight on the reasons for the different performances of the rainfall forecasts from these experiments. Our main findings from this study are summarized below:

1) Assimilating rainfall alone results in large but unrealistic temperature and humidity increments which enhances the rainfall forecast skill, as compared to the baseline experiment, in the first 3 h but degrades it thereafter, due to the lack of dynamical consistency.
2) While the radar data assimilation is critical for capturing the regional-scale wind circulation and associated updraft crucial for convective-scale heavy rainfall forecasts, it has little impact on humidity

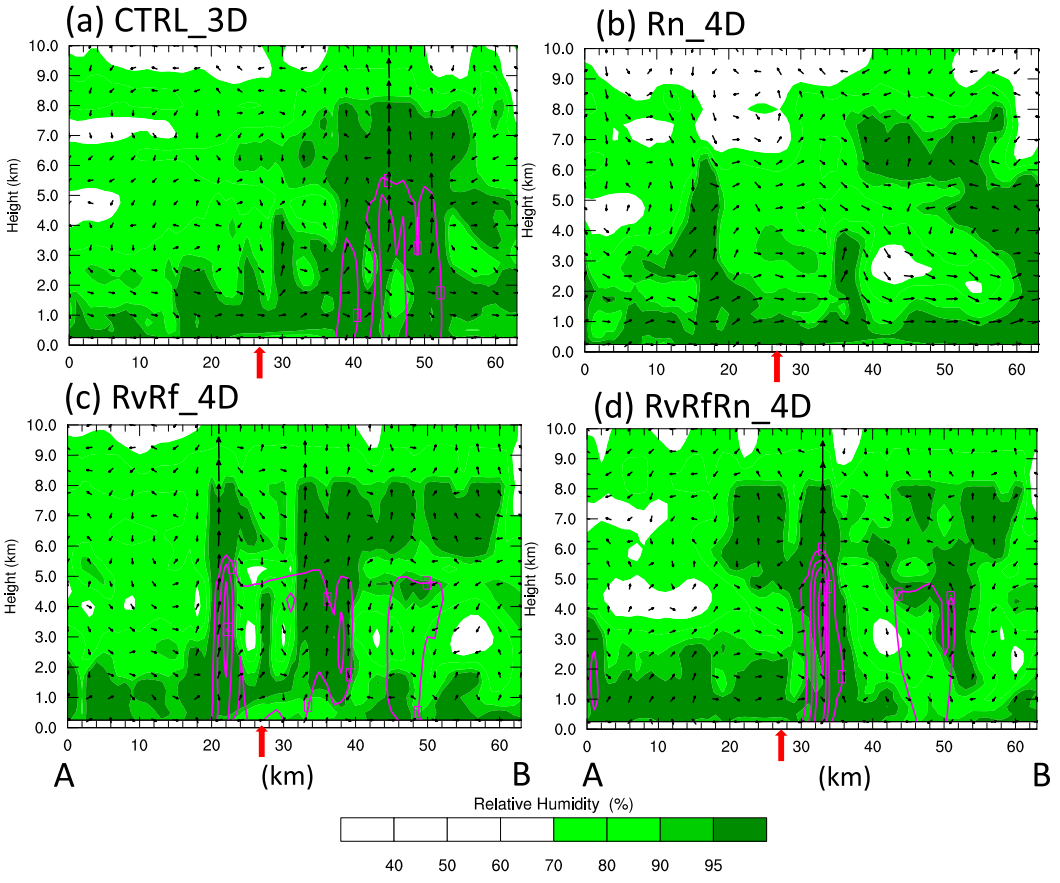

FIG. 18. As in Fig. 17, but for 2-h forecast (valid at 1700 UTC). The magenta contour lines are rainwater mixing ratio above 1 g kg^{-1} with an interval of 1.5 g kg^{-1}. The red arrows indicate the location of the observed rainfall maximum.

analysis that also plays a critical role for heavy rainfall prediction.

3) Assimilating the rainfall data in addition to the radar observations results in positive impact on heavy rainfall forecasts. The temperature and humidity responses resulting from the rainfall assimilation provide important thermodynamic information in the initial conditions in addition to the dynamical information from radar DA. The simultaneous assimilation of rainfall and radar eliminates the unrealistic large increments in the rainfall alone experiment.
4) Radar reflectivity DA plays a smaller role in the analysis fields of wind, temperature, and humidity in comparison to rainfall DA. The relative merit of rainfall DA is likely due to it only requires the model to produce a reasonable two-dimensional accumulated rainfall over a time period, which is less difficult for the model to achieve than an accurate temporal hydrometeor distribution as required by the reflectivity DA. Nevertheless, the inclusion of reflectivity in addition to rainfall and radial velocity results in a slightly positive impact on the precipitation forecasts.
5) Combined assimilation of radar and rainfall data results in analyses with dynamical and thermodynamical coupling that creates updrafts in saturated air columns, leading to improve convective forecasting.

Although our study is encouraging in that it provides a demonstration of the importance to combine the observations with similar scales for convective precipitation forecasts, we are fully aware that further evaluation with more convective cases is necessary to draw a general conclusion. One concern of the 4D-Var technique is about its computation efficiency. A multiresolution methodology that allows variable resolutions in different outer loop cycles has been developed at NCAR aiming to reduce the computation cost. Preliminary experiments produced encouraging results. The work will be reported in a separate paper.

It is noted in the current case study that even with the combined assimilation of radar and rainfall data the

heavy rainfall is still underpredicted. Research is under way to identify the errors sources (i.e., model errors, observation insufficiency and data assimilation strategy) that cause the underprediction. Assimilation of additional types of convective-scale observations, such as lightning detection networks, geostationary satellites, and crowdsourcing data all have the potential to help reduce the initial condition uncertainty of convection-permitting model leading to improved heavy rainfall prediction.

Acknowledgments. This research is based upon work supported by the National Center for Atmospheric Research, which is a major facility sponsored by the National Science Foundation under Cooperative Agreement 1852977. This research was also funded in part by the Central Weather Bureau (CWB), Taiwan Contract 50711.

REFERENCES

Albers, S. C., J. A. McGinley, D. L. Birkenheuer, and J. R. Smart, 1996: The Local Analysis and Prediction System (LAPS): Analyses of clouds, precipitation, and temperature. *Wea. Forecasting*, **11**, 273–287, https://doi.org/10.1175/1520-0434(1996)011<0273:TLAAPS>2.0.CO;2.

Ballard, S. P., Z. Li, D. Simonin, and J.-F. Caron, 2015: Performance of 4D-Var NWP-based nowcasting of precipitation at the Met Office for summer 2012. *Quart. J. Roy. Meteor. Soc.*, **142**, 472–487, https://doi.org/10.1002/qj.2665.

Ban, J., Z. Liu, X. Zhang, X.-Y Huang, and H. Wang, 2017:Precipitation data assimilation in WRFDA 4D-Var: Implementation and application to convection-permitting forecasts over United States, *Tellus*, **69A**, 1368310, https://doi.org/10.1080/16000870.2017.1368310.

Chen, G. T.-J., 2004: Research on the phenomena of Meiyu during the past quarter century: An overview. *East Asian Monsoon*, C.-P. Chang, Ed., World Scientific, 357–403.

——, and C.-C. Yu, 1988: Study of low level jet and extremely heavy rainfall over northern Taiwan in the mei-yu season. *Mon. Wea. Rev.*, **116**, 884–891, https://doi.org/10.1175/1520-0493(1988)116<0884:SOLLJA>2.0.CO;2.

Courtier, P., J.-N. Thépaut, and A. Hollingsworth, 1994: A strategy for operational implementation of 4D-Var, using an incremental approach. *Quart. J. Roy. Meteor. Soc.*, **120**, 1367–1387, https://doi.org/10.1002/qj.49712051912.

Dixon, K., C. F. Mass, G. J. Hakim, and R. H. Holzworth, 2016: The impact of lightning data assimilation on deterministic and ensemble forecasts of convective events. *J. Atmos. Oceanic Technol.*, **33**, 1801–1823, https://doi.org/10.1175/JTECH-D-15-0188.1.

Fabry, F., and J. Sun, 2010: For how long should what data be assimilated for the mesoscale forecasting of convection and why? Part I: On the propagation of initial condition errors and their implications for data assimilation. *Mon. Wea. Rev.*, **138**, 242–255, https://doi.org/10.1175/2009MWR2883.1.

Fierro, A. O., E. R. Mansell, C. L. Ziegler, and D. R. MacGorman, 2012: Application of a lightning data assimilation technique in the WRF-ARW model at cloud-resolving scales for the tornado outbreak of 24 May 2011. *Mon. Wea. Rev.*, **140**, 2609–2627, https://doi.org/10.1175/MWR-D-11-00299.1.

——, J. Gao, C. L. Ziegler, E. R. Mansell, D. R. MacGorman, and S. R. Dembek, 2014: Evaluation of a cloud-scale lightning data assimilation technique and a 3DVAR method for the analysis and short-term forecast of the 29 June 2012 derecho event. *Mon. Wea. Rev.*, **142**, 183–202, https://doi.org/10.1175/MWR-D-13-00142.1.

Gao, J., and D. J. Stensrud, 2012: Assimilation of reflectivity data in a convective-scale, cycled 3DVAR framework with hydrometeor classification. *J. Atmos. Sci.*, **69**, 1054–1065, https://doi.org/10.1175/JAS-D-11-0162.1.

Guo, Y.-R., Y.-H. Kuo, J. Dudhia, D. Parsons, and C. Rocken, 2000: Four-dimensional variational data assimilation of heterogeneous mesoscale observations for a strong convective case. *Mon. Wea. Rev.*, **128**, 619–643, https://doi.org/10.1175/1520-0493(2000)128<0619:FDVDAO>2.0.CO;2.

Heideman, K., and J. Fritsch, 1984: A quantitative evaluation of the warm-season QPF problem. Preprints, *Tenth Conf. on Weather Forecasting and Analysis*, Clearwater Beach, FL, Amer. Meteor. Soc., 57–64.

Honda, T., and Coauthors, 2018a: Assimilating all-sky *Himawaru-8* satellite infrared radiance: A cases of Typhoon Soudelor (2015). *Mon. Wea. Rev.*, **146**, 213–229, https://doi.org/10.1175/MWR-D-16-0357.1.

——, S. Kotsuki, G.-Y. Lien, Y. Maejima, K. Okamoto, and T. Miyoshi, 2018b: Assimilation of Hamawari-8 all-sky radiance every 10 minutes: Impact on precipitation and flood risk prediction. *J. Geophys. Res. Atmos.*, **123**, 965–976, https://doi.org/10.1002/2017JD027096.

Hu, M., M. Xue, and K. Brewster, 2006: 3DVAR and cloud analysis with WSR-88D level-II data for the prediction of the Fort Worth, Texas, tornadic thunderstorms. Part I: Cloud analysis and its impact. *Mon. Wea. Rev.*, **134**, 675–698, https://doi.org/10.1175/MWR3092.1.

Huang, X.-Y., and Coauthors, 2009: Four-dimensional variational data assimilation for WRF: Formulation and preliminary results. *Mon. Wea. Rev.*, **137**, 299–314, https://doi.org/10.1175/2008MWR2577.1.

Jones, C. D., and B. Macpherson, 1997: A latent heat nudging scheme for the assimilation of precipitation data into an operational mesoscale model. *Meteor. Appl.*, **4**, 269–277, https://doi.org/10.1017/S1350482797000522.

Jones, T. A., D. J. Stensrud, L. Wicker, P. Minnis, and R. Palikonda, 2015: Simultaneous radar and satellite storm-scale data assimilation using an ensemble Kalman filter approach for 24 May 2011. *Mon. Wea. Rev.*, **143**, 165–194, https://doi.org/10.1175/MWR-D-14-00180.1.

——, K. Knopfmeier, D. Wheatley, G. Creager, P. Minnis, and R. Palikonda, 2016: Storm-scale data assimilation and ensemble forecasting with the NSSL experimental warn-on-forecast system. Part II: Combined radar and satellite data experiments. *Wea. Forecasting*, **31**, 297–327, https://doi.org/10.1175/WAF-D-15-0107.1.

Kawabata, T., T. Kuroda, H. Seko, and K. Saito, 2011: A cloud-resolving 4DVAR assimilation experiment for a local heavy rainfall event in the Tokyo metropolitan area. *Mon. Wea. Rev.*, **139**, 1911–1931, https://doi.org/10.1175/2011MWR3428.1.

Koizumi, K., Y. Ishikawa, and T. Tsuyuki, 2005: Assimilation of precipitation data to the JMA mesoscale model with a four-dimensional variational method and its impact on precipitation forecasts. *SOLA*, **1**, 45–48, https://doi.org/10.2151/SOLA.2005-013.

Li, Z., Z. Pu, J. Sun, and W.-C. Lee, 2014: Impacts of 4D-VAR assimilation of airborne Doppler radar observations on numerical simulations of the genesis of Typhoon Nuri (2008).

J. Appl. Meteor. Climatol., **53**, 2325–2343, https://doi.org/10.1175/JAMC-D-14-0046.1.

——, S. P. Ballard, and D. Simonin, 2018: Comparison of 3D-Var and 4D-Var data assimilation in an NWP-based system for precipitation nowcasting at the Met Office. *Quart. J. Roy. Meteor. Soc.*, **144**, 404–413, https://doi.org/10.1002/qj.3211.

Lien, G.-Y., E. Kalnay, and T. Miyoshi, 2013: Effective assimilation of global precipitation: Simulation experiments. *Tellus*, **65A**, 19915, https://doi.org/10.3402/tellusa.v65i0.19915.

Lim, E., and J. Sun, 2010: A velocity dealiasing technique using rapidly updated analysis from a four-dimensional variational Doppler radar data assimilation system. *J. Atmos. Oceanic Technol.*, **27**, 1140–1152, https://doi.org/10.1175/2010JTECHA1300.1.

Lopez, P., 2013: Experimental 4D-Var assimilation of SYNOP rain gauge data at ECMWF. *Mon. Wea. Rev.*, **141**, 1527–1544, https://doi.org/10.1175/MWR-D-12-00024.1.

——, and P. Bauer, 2007: "1D+4DVAR" assimilation of NCEP stage-IV radar and gauge hourly precipitation data at ECMWF. *Mon. Wea. Rev.*, **135**, 2506–2524, https://doi.org/10.1175/MWR3409.1.

Miyoshi, T., and K. Aranami, 2006: Applying a four-dimensional local ensemble transform Kalman filter (4D-LETKF) to the JMA Nonhydrostatic Model (NHM). *SOLA*, **2**, 128–131, https://doi.org/10.2151/SOLA.2006-033.

Schumacher, R. S., and R. H. Johnson, 2005: Organization and environmental properties of extreme-rain-producing mesoscale convective systems. *Mon. Wea. Rev.*, **133**, 961–976, https://doi.org/10.1175/MWR2899.1.

Skamarock, W. C., and Coauthors, 2008: A description of the Advanced Research WRF version 3. NCAR Tech. Note NCAR/TN-475+STR, 113 pp., https://doi.org/10.5065/D68S4MVH.

Stephan, K., S. Klink, and C. Schraff, 2008: Assimilation of radar derived rain rates into the convective scale model COSMO-DE at DWD. *Quart. J. Roy. Meteor. Soc.*, **134**, 1315–1326, https://doi.org/10.1002/qj.269.

Sun, J., 2005: Initialization and numerical forecasting of a supercell storm observed during STEPS. *Mon. Wea. Rev.*, **133**, 793–813, https://doi.org/10.1175/MWR2887.1.

——, and N. A. Crook, 1997: Dynamical and microphysical retrieval from Doppler radar observations using a cloud model and its adjoint: Part I. Model development and simulated data experiments. *J. Atmos. Sci.*, **54**, 1642–1661, https://doi.org/10.1175/1520-0469(1997)054<1642:DAMRFD>2.0.CO;2.

——, and H. Wang, 2013: Radar data assimilation with WRF 4D-Var. Part II: Comparison with 3D-Var for a squall line over the U.S. Great Plains. *Mon. Wea. Rev.*, **141**, 2245–2264, https://doi.org/10.1175/MWR-D-12-00169.1.

——, and Coauthors, 2014: Use of NWP for nowcasting convective precipitation: Recent progress and challenges. *Bull. Amer. Meteor. Soc.*, **95**, 409–426, https://doi.org/10.1175/BAMS-D-11-00263.1.

——, H. Wang, W. Tong, Y. Zhang, D. Xu, and C.-Y. Lin, 2016: Comparison of the impacts of momentum control variables on high-resolution variational data assimilation and precipitation forecasting. *Mon. Wea. Rev.*, **144**, 149–169, https://doi.org/10.1175/MWR-D-14-00205.1.

Tong, W., J. Sun, G. Li, and X. Tang, 2016: Design strategies of an hourly update 3DVAR data assimilation system for improved convective forecasting. *Wea. Forecasting*, **31**, 1673–1695, https://doi.org/10.1175/WAF-D-16-0041.1.

Tsuyuki, T., K. Koizumi, and Y. Ishikawa, 2002: The JMA mesoscale 4D-Var system and assimilation of precipitation and moisture data. Proc. *ECMWF Workshop on Humidity Analysis*, Reading, United Kingdom, European Centre for Medium-Range Weather Forecasts, 59–67.

Wang, H., J. Sun, S. Fan, and X.-Y. Huang, 2013a: Indirect assimilation of radar reflectivity with WRF 3D-Var and its impact on prediction of four summertime convective events. *J. Appl. Meteor. Climatol.*, **52**, 889–902, https://doi.org/10.1175/JAMC-D-12-0120.1.

——, ——, X. Zhang, X.-Y. Huang, and T. Auligné, 2013b: Radar data assimilation with WRF 4D-Var: Part I. System development and preliminary testing. *Mon. Wea. Rev.*, **141**, 2224–2244, https://doi.org/10.1175/MWR-D-12-00168.1.

Weygandt, S. S., S. G. Benjamin, T. G. Smirnova, and J. M. Brown, 2008: Assimilation of radar reflectivity data using a diabatic digital filter within the Rapid Update Cycle. *12th Conf. on IOAS-AOLS*, New Orleans, LA, Amer. Meteor. Soc., 8.4, https://ams.confex.com/ams/88Annual/techprogram/paper_134081.htm.

Xiao, Q., Y.-H. Kuo, J. Sun, W.-C. Lee, E. Lim, Y. Guo, and D. M. Barker, 2005: Assimilation of Doppler radar observations with a regional 3D-Var system: Impact of Doppler velocities on forecasts of a heavy rainfall case. *J. Appl. Meteor.*, **44**, 768–788, https://doi.org/10.1175/JAM2248.1.

——, ——, ——, ——, D. M. Barker, and E. Lim, 2007: An approach of radar reflectivity data assimilation and its assessment with the inland QPF of Typhoon Rusa (2002) at landfall. *J. Appl. Meteor. Climatol.*, **46**, 14–22, https://doi.org/10.1175/JAM2439.1.

Xu, J., Q. Xiao, X. Gao, and S. Sorooshian, 2006: Influence of assimilating rainfall derived from WSR-88D radar on the rainstorm forecasts over the southwestern United States. *J. Geophys. Res.*, **111**, D13105, https://doi.org/10.1029/2005JD006650.

Xue, M., D.-H. Wang, J.-D. Gao, K. Brewster, and K. K. Droegemeier, 2003: The Advanced Regional Prediction System (ARPS), storm-scale numerical weather prediction and data assimilation. *Meteor. Atmos. Phys.*, **82**, 139–170, https://doi.org/10.1007/s00703-001-0595-6.

Zhang, J., and Coauthors, 2008: High-resolution QPE system for Taiwan. *Data Assimilation for Atmospheric, Oceanic, and Hydrologic Applications*, S. K. Park and L. Xu, Eds., Springer-Verlag, 147–162.

Zhang, X., X.-Y. Huang, and N. Pan, 2013: Development of the upgraded tangent linear and adjoint of the Weather Research and Forecasting (WRF) Model. *J. Atmos. Oceanic Technol.*, **30**, 1180–1188, https://doi.org/10.1175/JTECH-D-12-00213.1.

Zhang, Y., F. Zhang, D. Stensrud, 2018: Assimilating all-sky infrared radiance from *GOES-16* ABI using an ensemble Kalman filter for convection-allowing severe thunderstorms prediction. *Mon. Wea. Rev.*, **146**, 3363–3381, https://doi.org/10.1175/MWR-D-18-0062.1.

Zou, X., and Y. Kuo, 1996: Rainfall assimilation through an optimal control of initial and boundary conditions in a limited-area mesoscale model. *Mon. Wea. Rev.*, **124**, 2859–2882, https://doi.org/10.1175/1520-0493(1996)124<2859:RATAOC>2.0.CO;2.

Zupanski, D., S. Q. Zhang, M. Zupanski, A. Y. Hou, and S. H. Cheung, 2011: A prototype WRF-based ensemble data assimilation system for dynamically downscaling satellite precipitation observations. *J. Hydrometeor.*, **12**, 118–134, https://doi.org/10.1175/2010JHM1271.1.